ACCSCIENCE PUBLISHING

International Journal of Bioprinting

RESEARCH ARTICLE

Heterotopically differentiated PDLSCs-laden 3D-bioprinted scaffolds for concurrent oral hard and soft tissue regeneration

Huilin Zhu[1,2†], Ke Yi[1,2†], Zhihui Tang[1,2*],and Qing Li[1,2,3*]

[1] Second Clinical Division, Peking University School and Hospital of Stomatology, Beijing, China

[2] National Center for Stomatology and National Clinical Research Center for Oral Diseases and National Engineering Research Center of Oral Biomaterials and Digital Medical Devices, Beijing, China

[3] Center of Digital Dentistry, Peking University School and Hospital of Stomatology, Beijing, China

Abstract

Following dental extraction, the alveolar bone and gingival tissues could undergo varying degrees of resorption, which affects subsequent implant integration and aesthetic outcomes. Thus, having adequate volume of both hard and soft tissues for implantation or aesthetic restoration is essential for optimal results. Three-dimensional (3D) bioprinting technology offers the advantages of biomimicry, personalization, and precise spatial distribution, which are pivotal for enhancing the success and esthetics of dental restorations. In this study, we fabricated a construct with a natural transition and varying material concentrations by 3D bioprinting, comprising an upper layer of collagen/alginate/periodontal ligament stem cells (PDLSCs) and a lower layer of collagen/nano-hydroxyapatite (nHA)/alginate/PDLSCs. Characterization of the physicochemical properties revealed that the incorporation of nHA significantly enhanced the mechanical properties of both the bioink and the construct.Flow cytometry analysis confirmed the stemness of PDLSCs. Scanning electron microscopy (SEM) revealed that the construct possesses satisfactory pore density and a natural transition at the stratification point. The construct displayed good cell viability and proliferation, with the cellular movement observed at the stratification interface after bioprinting. Differentiation staining and quantitative reverse-transcription polymerase chain reaction (RT-qPCR) results demonstrated that PDLSCs within the 3D construct are capable of both osteogenic and fibroblastic differentiations. Ectopic transplantation in mice confirmed the biocompatibility of the construct. A rat tooth extraction model validated the construct's effectiveness in the integrated regeneration of both hard and soft tissues in alveolar ridge preservation. In conclusion, this personalized, concentration-varied 3D construct exhibits excellent biocompatibility and tissue preservation effects, holding significant potential for clinical application.

Keywords: 3D bioprinting; Heterotopic differentiation; Stem cells; Oral tissue engineering

†These authors have contributed equally to this work.

***Corresponding authors:**
Zhihui Tang (zhihui_tang@bjmu.edu.cn)

Qing Li (qingli@bjmu.edu.cn)

Citation: Zhu H, Yi K, Tang Z, Li Q. Heterotopically differentiated PDLSCs-laden 3D-bioprintedscaffolds for concurrent oral hard and soft tissue regeneration. *Int J Bioprint*. 2025;11(1):259-283. doi: 10.36922/ijb.4889

Received: September 19, 2024
1st revised: October 8, 2024
2nd revised: October 23, 2024
Accepted: October 24, 2024
Published Online: October 24, 2024

Copyright: © 2024 Author(s). This is an Open Access article distributed under the terms of the Creative Commons Attribution License, permitting distribution, and reproduction in any medium, provided the original work is properly cited.

Publisher's Note: AccScience Publishing remains neutral with regard to jurisdictional claims in published maps and institutional affiliations.

1. Introduction

The alveolar bone serves as the supportive structure for teeth, with the surface covered by gingival tissue. Following tooth extraction, both the alveolar bone and gingiva undergo a natural process of remodeling, generally resulting in a reduction in volume compared to the pre-extraction condition. Research suggested that within six months post-extraction, the extent of bone resorption is expected to range between 29% and 63% in width and 11% and 22% in height.[1] The resorption of hard and soft tissues may impede subsequent implant placement, particularly in the anterior region, where the deficiency in alveolar ridge dimensions may lead to suboptimal aesthetic outcomes.[2,3]

To mitigate the need for extensive bone and soft tissue augmentation procedures post-extraction, the concept of alveolar ridge preservation (ARP) has been introduced. The ARP technique involves the placement of bone substitutes in the alveolar socket, usually followed by a soft tissue graft.[4] The traditional ARP often employs graininess bone and autogenous soft tissues, involving complex procedures, extended clinical operation time, and a higher risk of postoperative complications. A review has highlighted that the combined use of bone and soft tissue substitutes in ARP is associated with increased treatment costs.[5] Three-dimensional (3D) bioprinting offers the potential to fabricate biomimetic, integrated hard and soft tissue structures to improve clinical outcomes. To enhance clinical efficiency and efficacy and to explore the effects of ARP, this article introduces a new integrated 3D-printed biomaterial.

Collagen has been extensively utilized in dental applications, such as membranes, bone institute materials, drug delivery systems, and hemostatic agents. It plays an important role in wound healing and angiogenesis, making it an ideal candidate for sealing wounds and closing extraction sites to facilitate healing.[6] Collagen-based membranes have been effective in periodontal and implant therapies, serving as barriers against epithelial migration.[7] A meta-analysis has demonstrated that crosslinked collagen membranes exhibit superior performance in restoring soft tissue thickness and height compared to other materials in ARP.[8] Nano-hydroxyapatite (nHA) serves as an ideal substitute for the inorganic component in natural bone minerals, boasting superior osteoinductive properties that render it advantageous for applications such as orthopedic implant coatings and bone substitute fillers.[9] The organic phase of bone tissue, predominantly composed of type I collagen, constitutes 90% of the bone composition, while the inorganic phase is primarily hydroxyapatite (HA).[10] The combination of HA and collagen is widely applied in the field of oral tissue regeneration. In clinical practice, ARP commonly involves the implantation of bone matrix materials, followed by the application of a collagen membrane over the top to facilitate the volumetric retention of both bone and soft tissues. Studies have demonstrated that the use of xenogeneic bone substitutes in conjunction with collagen membranes can effectively maintain bone structure following tooth extraction.[11,12] However, there remains a gap in the accessibility of an integrated material designed for the simultaneous regeneration of both hard and soft tissues in ARP.We integrated natural collagen with nHA to create a cohesive material, which is poised to facilitate future clinical applications.

The alveolar bone surface, characterized by compact bone, exhibits a gradual decrease in bone density with increasing depth.[13] The average content of HA in the trabecular bone is comparatively lower than that in the compact bone; therefore, 3D bioprinting technology can be used to mimic the variation in HA content within the alveolar bone by altering pore diameter density.[14] The gingival connective tissue is composed of a dense network of type I collagen fibers, providing rigidity to the gingiva and firmly attaching them to the alveolar bone.[15]

Periodontal ligament stem cells (PDLSCs) possess the multipotent ability to differentiate into cells of osteogenic and fibroblastic lineages.[16] In a pioneering study, Seo et al.[17] co-transplanted PDLSCs with HA scaffold into periodontal defects in mice, leading to the reconstruction of cementum and periodontal ligament-like structures. Previous studies on the construction of heterogeneous structures using 3D bioprinting have predominantly focused on the regeneration of articular cartilage and skin. Historically, layered structures in these studies have employed different types of cells, which were mixed with various materials to assess tissue regeneration outcomes.[18–21] Typically, when engineering tissues at different hierarchical levels, a blend of distinct cell types is employed. For instance, the construction of biomimetic tissues such as articular cartilage[21,22] and the muscle-tendon interface[23] demonstrates this approach. Therefore, the bidirectional differentiation of PDLSCs holds immense promise for applications in oral bone and soft tissue engineering. In previous studies, the differentiation capabilities of PDLSCs were primarily focused on osteogenic or fibroblastic applications,[24–26] with few researches having simultaneously leveraged the multi-lineage differentiation potential of these cells.[16] We have harnessed the multi-lineage differentiation advantages of PDLSCs, promoting their bidirectional differentiation within an integrated material, thereby proposing new possibilities for tissue regeneration and future clinical applications.

The extraction socket appears to be an excellent model for testing the integration of hard and soft tissue-printed

structures, offering the potential for further exploration into the simultaneous heterologous differentiation of stem cells and the biological effects of ARP. Consequently, the aim of this research is to design a macro and microporous structure that mimics the gradient variation of collagen/HA, and encapsulate heterotopically differentiated PDLSCs to manufacture a bioactive, integrated hard and soft tissue repair material for post-extraction sockets.

2. Materials and methods

2.1. Bioink preparation and characterization

2.1.1. Cell preparation

Healthy periodontal tissues were extracted from orthodontic teeth or impacted third molars removed from adults aged 18–25. PDLSCs were isolated using an enzymatic digestion method. The study was approved by the Ethics Committee of the Peking University School and Hospital of Stomatology (PKUSSIRB-201950166), and all patients provided informed consent for sample collection. The cell proliferation medium (PM) consisted of α-MEM (Gibco, USA) supplemented with 10% fetal bovine serum (NOVA Medical Science and Technology Co., Ltd., Shanghai, China) and 1% Penicillin-Streptomycin-Amphotericin B Solution (Analysis Quiz, Beijing, China). Cells were cultured in this medium at 37°C in a 5% CO_2 incubator, with the medium replaced every 2–3 days. Once 80% confluence was reached, the cells were subcultured using 0.25% trypsin-EDTA (Gibco, USA). The osteogenic differentiation medium (OM) for PDLSCs was freshly prepared immediately before use, containing 100 nM dexamethasone (Sigma–Aldrich Co., Germany), 50 mM L-ascorbic acid (Sigma–Aldrich Co., Germany), and 10 mM β-glycerophosphate (Sigma Aldrich Co., Germany). All PDLSCs were used within five passages post-isolation.

2.1.2. Bioink preparation

The bioinks were categorized into two groups: collagen/alginate (CA) and collagen/nHA/alginate (CHA). Type I bovine tendon collagen sponges (Collagen Biotechnology Co. Ltd., China) were dispersed at a concentration of 0.03g/mL in 0.05mol/L acetic acid to prepare the collagen ink. nHA particles, with an average size of 60–80 nm and a molecular weight of 502.31 (Macklin Biochemical Co. Ltd., Shanghai, China), were incorporated into the collagen gel and continuously stirred at 45 rpm at 4°C for 12 hours to obtain the collagen/nHA bioink. Both bioinks were uniformly mixed with 10% alginate (Cat no. 180947; Sigma Aldrich, Germany) for subsequent Ca^{2+}crosslinking in 3D constructs. A macroscopic photograph of the prepared bioinks is presented (Figure 1a). The PDLSC-laden bioinks were fabricated by gently mixing PDLSCs (1×10^6cells/mL) with the CA and CHA inks.

2.1.3. Rheological analysis

The rheological properties of various bioinks were evaluated using a rotational rheometer (Discovery HR2; TA Instruments, Inc., USA) to assess their storage modulus (G′), loss modulus (G″), and complex viscosity. After applying a 0.6 Pa pressure for one minute, the bioinks reached equilibrium. Liquid, acellular bioinks were loaded onto the Peltier stage for individual measurements, with each sample undergoing a single test before disposal. Oscillatory temperature sweeps from 4°C to 35°C at a rate of 1.5°C/min were performed, with a duration of 10 minutes, and stress sweeps from 0.1 to 1000 Pa were conducted at a frequency and strain of 1 Hz and 1%, respectively. Strain sweeps (from 0.01% to 1%) were carried out at a fixed frequency of 1 Hz, while frequency sweeps (from 0.1 to 100 Hz) were performed at a fixed strain of 1%. To determine whether the viscosity of the bioinks decreases over time under shear, steady-state shear measurements were conducted at shear rates ranging from 0.1 to 100 s^{-1}.

2.1.4. Attenuated total reflectance-Fourier transform infrared spectroscopyanalysis

Chemical compositions of the CA and CHA bioinks were analyzed using an attenuated total reflectance-Fourier transform infrared spectroscopy (ATR-FTIR) (Bruker, Germany), within the spectral range of 500 to 4000 cm^{-1} at a resolution of 4 cm^{-1}. Each sample was directly analyzed on the ATR accessory equipped with a diamond crystal. A total of 32 scans were performed for each sample.

2.1.5. Thermogravimetric analysis

The thermal stability of the samples was assessed using thermogravimetric analysis (TGA) performed on a Thermal Gravimetric Analyzer (TA Instruments, Newcastle, DE, USA). The temperature was ramped at a rate of 10°C per minute, starting from 0°C and reaching up to 300°C. Throughout the heating process, a continuous purge of nitrogen gas at a flow rate of 100 mL/min was maintained. The spectral data were collected using the Q600 software (TA Instruments).

2.1.6. Flow cytometric analysis

Flow cytometry was employed to assess the presence and abundance of surface markers in the extracted cells. The analysis aimed to detect the presence of mesenchymal markers CD29, CD90, and CD146, characteristic of PDLSCs, while also evaluating the absence of CD45 and STRO-1, which further confirms the stem cell phenotype. Following the second passage, when the cells reached approximately 80% confluence, they were treated with 0.25% trypsin/EDTA, enumerated, and then resuspended in a 1% bovine serum albumin (BSA) solution to prepare a cell suspension at a concentration of 1×10^6 cells/mL.

Fluorescent antibody dyes specific for human CD29, CD45, CD90, CD146, and STRO-1 (1:20 dilution; Proteintech, USA) were added to the cell suspension and incubated in the dark at 4°C for 30 minutes. Post-washing, the cells were resuspended in 1% BSA and analyzed using a flow cytometer (TY2021001557, NovoCyte, USA). The analysis included the collection of 10,000 fluorescently labeled cells to ensure sufficient data for statistical analysis.

2.2. Preparation for 3D-bioprinting constructs

2.2.1. 3D bioprinting

The fabrication of 3D-printed constructs was performed using an extrusion-based 3D bioprinter (BMP-C300-T300-IN3, Medprin, China). During the printing process, nozzles with an inner diameter of 160–210μm were utilized for the extrusion of CA and CHA bioinks. The hydrogel was successfully extruded into fine filaments under a pressure of 0.15 MPa (Figure 1b). The extrusion of hydrogel was hard with nozzles having an inner diameter less than 160μm, and when the nozzle diameter was too large, the hydrogel dropped, due to gravity, in droplet form. A 3D structure with varying densities was designed using SOLIDWORKS 2024 (Dassault Systems, USA) to create a continuous construct with a gradient of density from top to bottom. Prior to printing, the designed cuboid model was imported into the printer as a stereolithography file and converted into slices by the MP Bioprint-v41 software (Figure 1c). The construct consisted of 10 layers, with the upper 5 layers made of CA and the lower 10 layers made of CHA, whose upper 3 layers had a denser structure, while the lower 7 layers were more sparse, thus forming a density-varying printed structure that affects the distribution of nHA content. Both types of bioinks were loaded into two separate sterile 1 mL syringes and uniformly mixed with PDLSCs. The co-axial printing function was employed, with the syringe containing CA bioink printing the upper structure and the one with CHA bioink printing the lower structure (Figure 1d). The bioinks were extruded along the X-Y path of each layer and transitioned to the Z-axis at the end of each layer.

After multiple rounds of printing trials, the printing parameters were optimized (Table 1) to ensure the reproducibility of the printing process and to maximize cell viability. Once the construct was printed, it was crosslinked at room temperature using a 50 mM sterile calcium chloride ($CaCl_2$) solution for 10 minutes. Subsequently, it was rinsed with phosphate-buffered saline (PBS) to remove any residual $CaCl_2$ and then transferred to a PM for further cultivation.

2.2.2. Compressive modulus analysis

Given that the primary load-bearing mechanism for bone and soft tissues is compression[27] our study focused on the behavior of constructs under compressive loading. CA, CHA, and CA/CHA constructs of appropriate dimensions (10 mm × 10 mm × 5 mm) were fabricated, and their length, width, and thickness were manually verified using a vernier caliper. The compression tests were conducted using a universal testing machine (Instron Model 3342, Illinois Tool Works, Inc., MA, USA). Samples were placed between the load-bearing sensors of a circular metal plate and compressed at a rate of 0.5 mm/min to a deformation of 80%, with their compression displacement and the corresponding force values being recorded.

Table 1. The printing parameters of the extrusion-based 3D bioprinting

Group	Platform temperature (°C)	Pressure (MPa)	Speed (mm/s)	Needle gauge (G)
CA	4	0.15	8	30
CHA	4	0.15	8	27

Abbreviations: CA: Collagen/alginate; CHA: Collagen/nano-hydroxyapatite/alginate.

2.2.3. Scanning electron microscopy analysis

The microstructure of the constructs was examined using field-emission scanning electron microscopy (FESEM; Model S-4800; Hitachi High-Technologies Co., Tokyo, Japan). All samples were coated with a thin layer of platinum via sputtering to enhance the resolution of the micrographs. Subsequently, the gold-sputtered samples were observed under an acceleration voltage of 3 kV.

2.3. *In vitro* study

2.3.1. Cell viability assay

A live/dead cell staining kit (KeyGEN Biotech Co., Jiangsu, China) was employed to assess cell viability within the CA and CHA constructs on days 1, 4, and 7 post-printing. The constructs were incubated in a solution containing 8 μM propidium iodide and 2 μM calcein-AM for a period of 30–45 minutes. After incubation, the working solution was aspirated to terminate the staining process, and the samples were then examined using an inverted fluorescence microscope (Olympus, Japan).

2.3.2. Cell proliferation analysis

The Cell Counting Kit-8 (CCK-8; Analysis Quiz, Beijing, China) was utilized to assess cell proliferation within the CA and CHA constructs on days 1, 3, 5, and 7 post-printing. To mitigate the interference of the materials with the CCK-8 reagent, which could affect the experimental outcomes, healthy PDLSCs were cultured with the material extract. A 12-transwell plate was employed to co-culture the adherent cells with the material, with a fixed amount of material added to each well chamber and culture

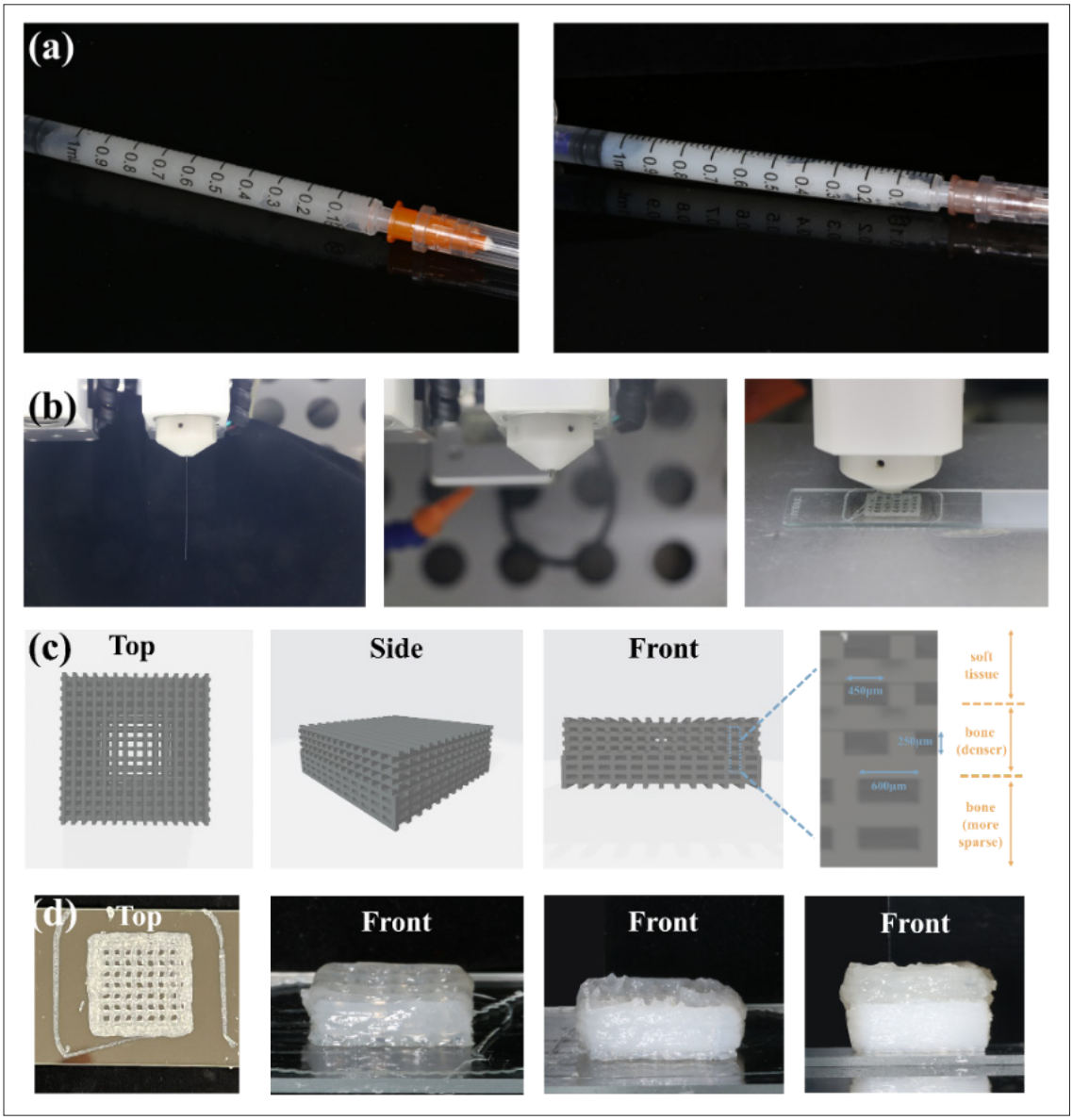

Figure 1. Macroscopic images of bioinks, bioprinting processes, and constructs. (a) The macroscopic appearance of the CA bioink (left) and the CHA bioink (right) within a 1 mL syringe. (b) The extrusion of fine filaments during printing (left), the inability to extrude the bioink when the nozzle diameter is too small (middle), and the ongoing printing process (right). (c) The designed 3D construct model with stratified layers, viewed from the top, side, and front. The upper layer of the lattice is designed with a pore size of 450 μm, and the lower layer, characterized by a more open structure, has lattice dimensions of 600 μm. The diameter of the filament employed is 250 μm. (d) Macroscopic photographs of the printed construct, viewed from the top and front. Abbreviations: CA: Collagen/alginate; CHA: Collagen/nano-hydroxyapatite/alginate.

medium added to submerge the material, with medium changes occurring every 48 hours. At the designated testing time, the CCK-8 reagent was added to the wells, and after a 2-hour incubation at 37°C, the supernatant was transferred to a 96-well plate. The optical density at 450 nm was measured using a microplate reader (BioTek ELX800, VT, USA). Cells without material stimulation served as the control group, with three replicates (n = 3).

2.3.3. Fluorescent staining of living cells

To determine whether cells at the transition between CA and CHA materials can migrate naturally, a live-cell fluorescence staining technique was employed to track cell locations. Cells were suspended in serum-free α-MEM medium at a concentration of 1×10^6 cells/mL and mixed with a live-cell fluorescent dye at a concentration of 5 μl/mL, then incubated at 37°C in the dark for 15 minutes. Cells intended for the CA bioink were stained with VybrantTM

DiO (Thermo Scientific, USA), while those for the CHA bioink were stained with VybrantTM DiD (Thermo Scientific, USA). As previously described, a construct with an upper layer of CA and a lower layer of CHA was printed using bioprinting technology and cultured in PM under dark conditions until day 7. The transition section of the material was then sectioned longitudinally and examined using a scanning electron microscope and an inverted fluorescence microscope to capture the cellular fluorescence imaging.

2.3.4. Alkaline phosphatase staining

An alkaline phosphatase (ALP) staining kit (Solarbio, Beijing, China) was employed to visualize ALP within cells based on the azo-coupling method, thereby assessing the osteogenic potential of PDLSCs within CHA constructs. Cells were cultured for 14 days using the CHA material extract stimulation method as described in Section 2.3.2. To validate the effectiveness of the custom-made OM, control groups were established with PDLSCs cultured in regular PM and OM without material stimulation. The experimental group was cultured with PDLSCs under material co-stimulation using the OM. To explore the osteogenic effect of the CHA material itself, an additional experimental group was included, where PDLSCs were cultured in regular medium under material co-stimulation. On the 7th and 14th days of culture, the medium was removed from the wells, and the cells were fixed for 1 minute with pre-cooled ALP fixative at 4°C. After rinsing with PBS, ALP incubation solution was added to cover the cells, followed by a 20-minute incubation at 37°C, and then rinsed with PBS. Finally, cells were counterstained with methyl green for 5 minutes, and the results were documented with photography.

2.3.5. Picro Sirius Redstaining

The fibroblastic differentiation of PDLSCs within CA constructs was evaluated using Picro Sirius Redstaining solution (Sigma–Aldrich Co., Germany). The experimental group design followed the same protocol as the ALP staining procedure. Cells in the well plates were fixed with 4% paraformaldehyde for 10 minutes, then rinsed with PBS. Afterward, the cells were submerged in Picro Sirius Reddye and incubated at room temperature for 60 minutes. The stain was aspirated, and the samples were rinsed twice with 0.5% acetic acid solution, followed by three rinses with anhydrous alcohol to dehydrate the samples. The final step involved photographing the results.

2.3.6. Quantitative reverse-transcription polymerase chain reaction

Quantitative reverse-transcription polymerase chain reaction (RT-qPCR) was employed to determine the transcriptional levels of specific genes in PDLSCs on the 7th and 14th days post-printing. Cells cultured with either CA or CHA material extract were collected from the well plates. Total RNA was extracted using the Trizol reagent (Invitrogen, USA) following the manufacturer's recommended protocol. Reverse transcription was performed using the PrimeScriptTM RT Reagent Kit (TaKaRa, Japan), and RT-qPCR was conducted with the FastStart Universal SYBR Green Master (Roche, Germany). Primer sequences are listed in Table 2. The expression levels of *COL1*, *ALP*, *RUNX2,* and *OPN* in PDLSCs stimulated by CHA material were assessed, as well as the expression levels of *COL1*, *PLAP1*, *FSP1,* and *ELASTIN* in PDLSCs stimulated by CA material. *GAPDH* served as an endogenous control, and the fold-difference was calculated using the $2^{-\Delta\Delta Ct}$ method, with triplicate samples ($n = 3$).

2.4. *In vivo* study

2.4.1. Biocompatibility analyses

In accordance with the ethical principles of the Laboratory Animal Research Ethics Committee of Peking University Health Science Center (Approval No.: DLASBD0054), constructs were implanted subcutaneously into 6- to 8-week-old male BALB/c nude mice (Charles River Laboratories, USA) to assess the biocompatibility of the 3D constructs. One week prior to the study, the animals were housed in two separate ventilated cages within an isolated specific pathogen-free (SPF) unit. The implants were categorized into two groups: acellular printed CHA and cellular printed CHA. Each animal was designated as an individual experimental unit. To ensure the reproducibility and reliability of the animal model data, six nude mice were selected for each group.

All instruments utilized in the procedure were sterilized using Cobalt-60 (Co-60) gamma radiation, ensuring aseptic conditions during surgery, which was conducted inside a laminar flow hood. Male BALB/c nude mice, aged 6–8 weeks and weighing approximately 20–25g ($n = 12$), were randomly assigned to two groups. Anesthesia was induced and maintained using isoflurane gas (RWD, China). A 10 cm longitudinal incision was made on the dorsal side of each mouse, and an implant (10 mm × 10 mm × 2 mm) was inserted subcutaneously. The incision was then closed with absorbable sutures. Following the procedure, the anesthesia was discontinued, and the mice were returned to their cages for further observation.

At the 2nd, 4th, and 8th weeks post-implantation, the nude mice were euthanized using an overdose of anesthesia. Macroscopic photographs of the subcutaneous constructs were taken to assess vascular ingrowth and the extent of *in vivo* absorption. The constructs were then

Table 2. Primers for *GAPDH*, *COL1*, *ALP*, *RUNX2*, *OPN*, *ELASTIN*, *FSP1*, and *PLAP1*.

Gene	Primer sequence (5' to 3')
GAPDH	Forward: GCACCGTCAAGGCTGAGAAC Reverse: ATGGTGGTGAAGACGCCAGT
COLI	Forward: CTGACCTTCCTGCGCCTGATGTCC Reverse: GTCTGGGGCACCAACGTCCAAGGG
ALP	Forward: TCAGAAGCTAACACCAACG Reverse: TTGTACGTCTTGGAGAGGGC
RUNX2	Forward: TCTGGCCTTCCACTCTCAGT Reverse: GACTGGCGGGGTGTAAGTAA
OPN	Forward: TCACCTGTGCCATACCAGTTAA Reverse: TGAGATGGGTCAGGGTTTAGC
ELASTIN	Forward: AAAGCAGCAGCAAAGTTCGG Reverse: ACCTGGGACAACTGGAATCC
FSP1	Forward: AGCTTCTTGGGGAAAAGGAC Reverse: CCCCAACCACATCAGAGG
PLAPI	Forward: CGATACAAAGAACTACAAAGGCTGG Reverse: GCATTTCCCAGTATTTCACCG

excised and fixed in a 4% paraformaldehyde solution for 24 hours, followed by dehydration and paraffin embedding. Sections were obtained by cutting perpendicular to the flap, and these were subjected to hematoxylin and eosin (HE) staining and Masson's trichrome staining for further histological evaluation.Following the implantation procedure, the number of capillaries within the material-embedded regions in the sections was counted under an optical microscope. Capillaries were defined as blood vessels with a diameter of less than 20 μm. Utilizing a microscope at a magnification of 20×, the number of capillaries was calculated for five random fields of view within the experimental area of each section in each group.

2.4.2. Evaluation of tissue regeneration effectiveness

In compliance with the ethical guidelines of the Laboratory Animal Research Ethics Committee of Peking University Health Science Center (Approval No.: DLASBD0054), constructs were implanted into the extraction sockets of the maxillary first molars (M1) in 6- to 8-week-old male nude rat to evaluate their efficacy in promoting hard and soft tissue regeneration at the extraction sites. Two weeks prior to the study, the animals were housed in two separate ventilated cages within an isolated SPF unit. The implants were categorized into three groups: acellular stratified printed CA/CHA, cellular printed CHA, and stratified cellular printed CA/CHA. Each mouse underwent extraction of the first molars on both the left and right maxillary sides, with each extraction site serving as an individual experimental unit. Each group's experiment was replicated three times. The control group consisted of extraction sites allowed to heal naturally without intervention.

All surgical instruments were sterilized using Co-60 gamma radiation to ensure aseptic conditions, and the surgical procedures were conducted within a laminar flow hood. Male nude mice, aged 6–8 weeks and weighing approximately 300–400 grams (n = 12), were randomly assigned to four groups.

Anesthesia was induced and maintained using isoflurane gas. After the complete extraction of the maxillary first molars on both the left and right sides, the implants were placed into the alveolar sockets and secured with absorbable sutures. Following the surgical intervention, the anesthesia was discontinued, and the mice were returned to their cages for subsequent observation and monitoring.

At weeks 4 and 8 post-surgery, the mice were euthanized by means of an overdose of anesthesia. The soft and hard tissue blocks at the extraction sites were excised and fixed in a 4% paraformaldehyde solution for 24 hours. Micro-computed tomography (micro-CT) scanning (SkyScan1276, Bruker, China) was performed to capture the sample structures, and the raw images obtained were processed and analyzed using CTAnalyser-CTvol and CTAnalyser-CTvox software (Bruker, China) to compare differences among the groups. The region of interest was defined using the CTAnalyser-CTAn software for 3D evaluation, which analyzed and measured the images based on grayscale to calculate the bone volume-to-tissue volume (BV/TV) ratio.[28]

Subsequently, the samples were dehydrated and embedded in paraffin. Sections were cut parallel to the longitudinal axis of the teeth to a thickness of 5 mm and stained with HE as well as Masson's trichrome stain for histological examination. Additionally, immunohistochemical (IHC) staining was performed on the samples using markers for CD31, BSP, OPN, COL-1, CTGF, and COL-3 to assess specific biological processes and tissue characteristics.

2.5. Statistical analysis

Data derived from triplicate experiments to ensure reproducibility are presented as mean ± standard deviation. The statistical analysis was conducted using SPSS software version 29.0 (IBM, USA). For comparisons between the two groups, a t-test was employed. A p-value of less than 0.05 was considered statistically significant.

3. Results

3.1. Preparation and characterization of bioinks

3.1.1. Rheological characterization

Investigating the rheological properties of bioinks is crucial for evaluating their printability. We assessed the storage modulus (G′) and loss modulus (G″) of CA and CHA bioinks at 4°C as a function of frequency (Figure 2a). Both G′ and G″ increased with increasing frequency. Throughout the entire frequency range, G′ consistently exceeded G″, indicating a gel-like behavior with a predominance of elastic characteristics. The CA bioink exhibited lower moduli, suggesting better flowability compared to the CHA bioink, which could account for the use of a smaller inner diameter nozzle for the CA bioink. At a given frequency, the incorporation of nHA particles increased the loss modulus and significantly enhanced the storage modulus, thereby improving the mechanical properties.

We further investigated the viscosity of the bioinks as a function of temperature and shear rate. Our findings indicated that the viscosity of the bioinks gradually decreases with the increase in temperature (Figure 2b). At a constant temperature, the incorporation of nHA was observed to enhance the viscosity of the bioinks. Beyond a critical temperature threshold of 45°C, the viscosity rapidly decreased. Within the initial temperature range of 4–25°C, the controlled rate of viscosity reduction was favorable for the execution of 3D printing. An increase in shear rate resulted in a significant reduction in viscosity, highlighting the pronounced shear-thinning behavior of both CA and CHA bioinks (Figure 2c). The viscosity of the CA and CHA bioinks was found to be quite similar, exhibiting closely matched shear-thinning characteristics. The addition of nHA, under the same shear rate conditions, was noted to augment the viscosity of the bioinks. Adjusting the shear rate to reduce the viscosity facilitates the extrusion of the bioinks, which is beneficial in protecting the cells from the detrimental effects of shear stress.[29]

3.1.2. ATR-FTIR analysis

Figure 2d presents the ATR-FTIR spectra of CA and CHA bioinks. The spectrum of CHA exhibited characteristic peaks of collagen and HA.[30] The amide I peak was located at 1633 cm^{-1}, corresponding to the carbonyl (C=O) stretching vibration, and the amide II peak was observed at 1529 cm^{-1}, indicative of the N-H bending vibration. The amide III peak was found in the vicinity of 1200 cm^{-1}, also associated with N-H bending vibrations. The presence of nHA was evidenced by the phosphate ($PO4^{3-}$) stretching bands within the range of 570–610 cm^{-1}. The results indicated

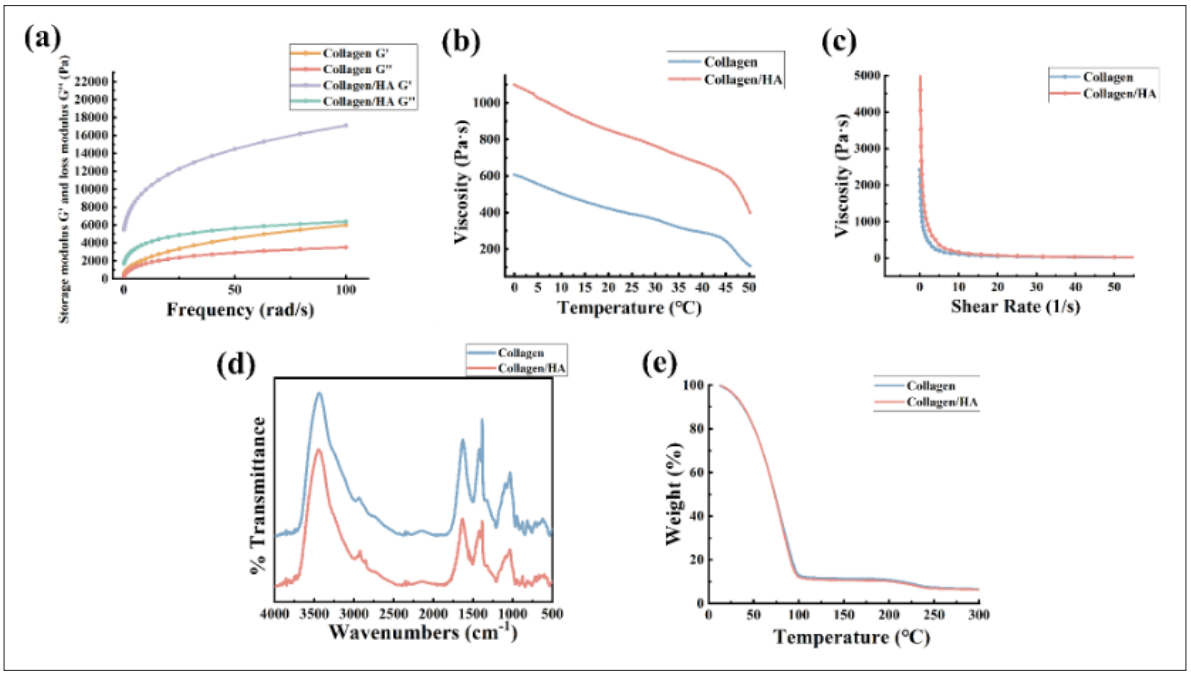

Figure 2. Characterization of physicochemical properties of the bioinks. (a) Rheological frequency sweep tests were conducted on both CA and CHA bioinks at 4°C, where G' denotes the storage modulus and G" represents the loss modulus. (b) The variation in viscosity of the two bioinks across different temperatures. (c) Illustration of the changes in viscosity of the bioinks under various shear rates. (d) The ATR-FTIR spectroscopic analysis of the bioinks reveals their chemical composition. (e) The TGA of the bioinks provides insights into their thermal stability. Abbreviations: ATR-FTIR: Attenuated total reflectance-Fourier transform infrared spectroscopy; HA: Hydroxyapatite; TGA: Thermogravimetric analysis.

that the incorporation of nHA did not affect the chemical structure of the collagen component.

3.1.3. TGA

TGA of the bioinks has confirmed that the weight loss of both bioinks is nearly synchronized under the influence of temperature (Figure 2e). Within the physiological temperature range of 37°C, the weight loss of the bioinks was minimal, which is advantageous for *in vivo* studies. The results indicated that due to thermal decomposition, the bioinks decomposed at temperatures exceeding 95°C. Consequently, all subsequent material sterilization was performed using gamma irradiation with a Co-60 source.

3.1.4. Flow cytometric analysis

Flow cytometry was employed to analyze the surface markers of PDLSCs, a critical step in characterizing their stem cell properties (Figure 3). The expression of CD29 and CD90, both positive, is indicative of mesenchymal stem cell (MSC) characteristics, and CD146 serves as a basis for identifying PDLSCs. Consistent with other MSCs, the majority of PDLSCs in culture exhibited negativity for CD45 (0.08% ± 0.02%) and STRO-1 (1.34% ± 0.09%). The analysis found that PDLSCs could express MSC-specific surface markers, including CD29 (99.86% ± 0.23%), CD90 (99.96% ± 0.05%), and CD146 (47.1% ± 0.36%). These findings suggested that the PDLSCs isolated from human teeth in this study possess the stemness of MSCs and were free from contamination by endothelial cells or hematopoietic stem cells.

3.2. Preparation and characterization of 3D constructs

3.2.1. Compressive modulus analysis

The stress-displacement curves (Figure 4a) and stress-strain curves (Figure 4b) of the 3D constructs demonstrated that the CHA/CA composite required a greater force to achieve the same degree of deformation compared to the CA construct, which exhibited the lowest compressive force required. This indicated that the incorporation of nHA enhanced the mechanical properties of the scaffold, and the layered CHA/CA scaffold's mechanical strength was conducive to subsequent *in vitro* and *in vivo* testing. The mechanical strength of the construct is also observable macroscopically in **Video S1** (see supplementary material).

3.2.2. Morphological analysis of 3D constructs

The microstructure of the construct's lattice framework was examined under SEM. Two distinct pore densities were

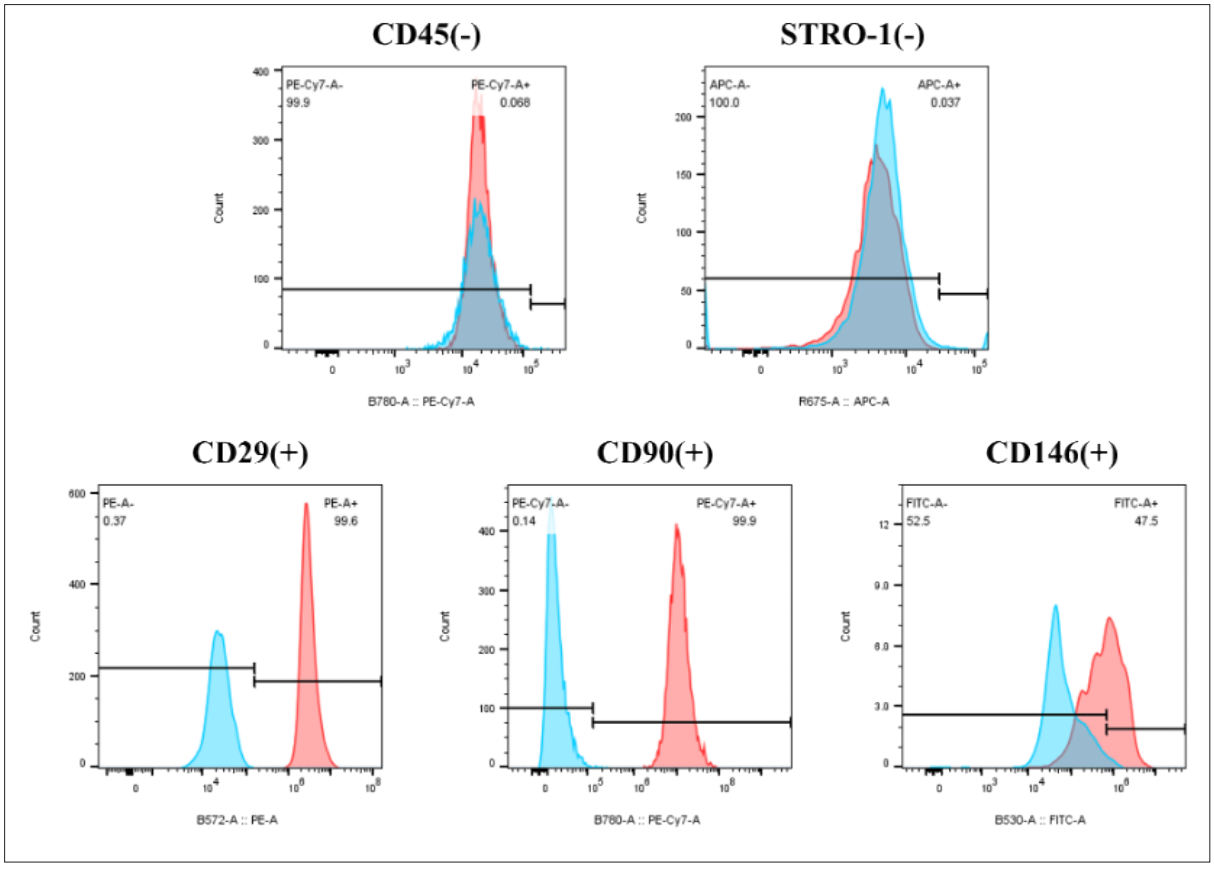

Figure 3. Flow cytometric analysis of PDLSCs based on characterization of stem cell markers: CD29 (+), CD90 (+), CD146 (+), CD45 (-), and STRO-1 (-).

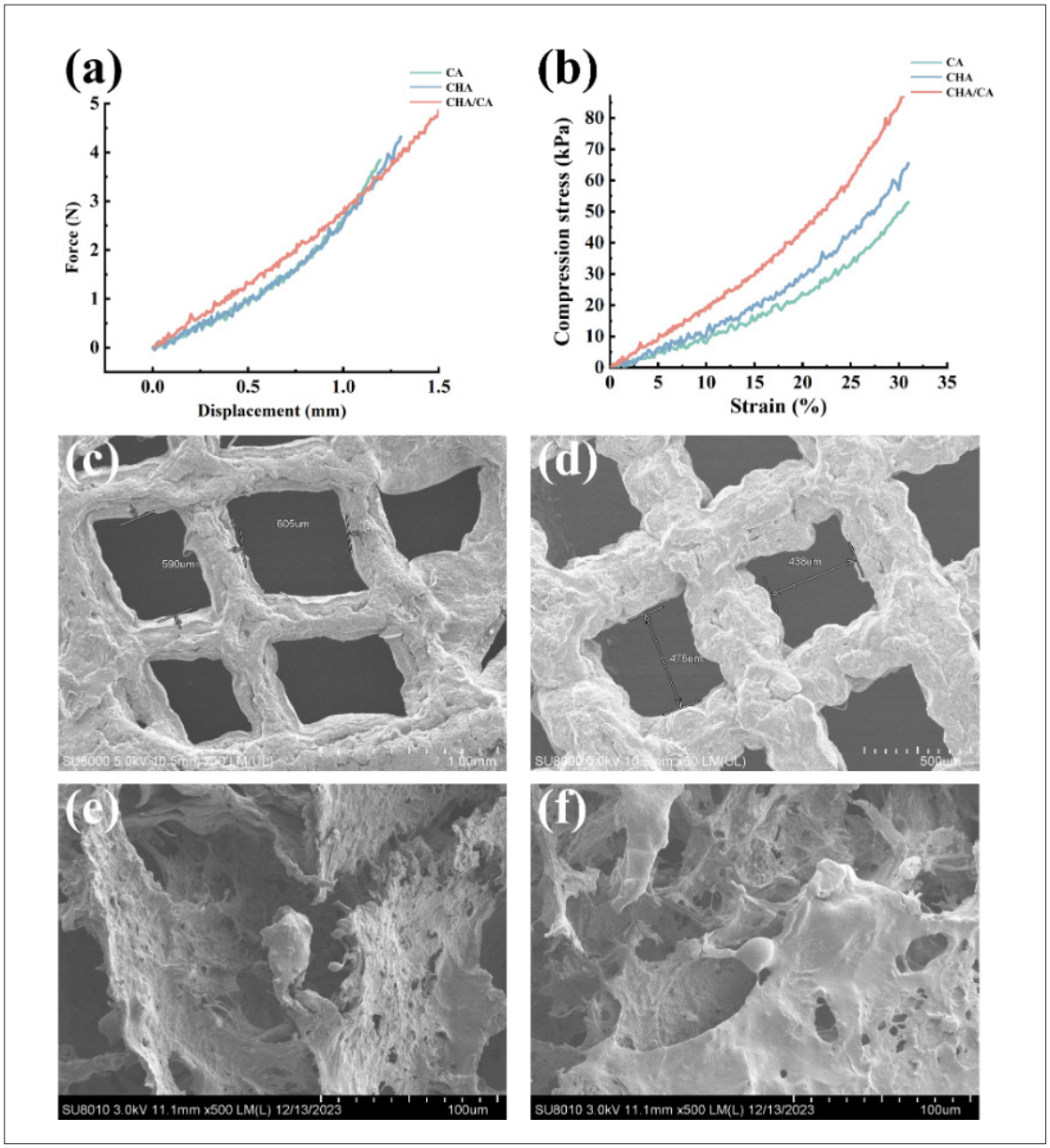

Figure 4. Mechanical properties and surface structure of the construct. (a) The force-displacement curves of the constructs. (b) The stress-strain curves of the constructs. (c) SEM image showinglarger pore sizes ofthe constructs near the bone tissue region, with macroscopic pore dimensions ranging from 550 to 600 μm. (d) SEM image showing smaller pore sizes ofthe constructs near the soft tissue region, with macroscopic pore dimensions ranging from 450 to 500 μm. (e) SEM image showing a micro-porous configuration in the microstructure of the construct near the bone tissue region. (f) SEM image showing a micro-porous configuration in the microstructure of the construct near the soft tissue region. Abbreviations: CA: Collagen/alginate; CHA: Collagen/nano-hydroxyapatite/alginate; SEM: Scanning electron microscopy.

designed for the construct to accommodate variations in the nHA content. The pore size in the region proximal to the bone tissue was tailored to be 550–600 μm (Figure 4c). In the region adjacent to the soft tissue, the pore size was reduced to 450–500 μm (Figure 4d). The microscopic findings confirmed that both types of constructs exhibited a porous structure, which is essential for enhanced cell infiltration and tissue integration (Figure 4e and 4f).

3.3. *In vitro* study

3.3.1. Cell viability

The cell viability within the constructs was assessed using a live/dead fluorescent staining method after 1, 4, and 7 days of *in vitro* culture, with the results depicted in Figure 5a. The 3D-printed constructs encapsulated the cells uniformly within the material, demonstrating high levels of cell viability sustained over the 7 days. Compared

to day 1, there was a significant increase in the density of live cells within the constructs.

3.3.2. Cell proliferation

Cell proliferation exhibited an upward trend throughout the culture period of 1, 3, 5, and 7 days, as shown in Figure 5b. At each measured time point, the optical density (OD) values for both the CHA and CA groups were higher than those of the control group, indicating enhanced cell growth in these groups. Notably, the proliferation rate of cells in the experimental groups peaked between days 5 and 7, suggesting an optimal period for cell expansion.

3.3.3. Fluorescent staining of living cells

To validate the natural transition between the two layers, we sectioned the transition zone longitudinally for both macroscopic and microscopic SEM observations. As illustrated in the previous macroscopic images of the materials, the upper construct composed of CA exhibited a translucent appearance, while the lower construct made of CHA appeared white (Figure 5c). SEM analysis revealed a seamless interface at the transition, indicating a tight connection between the two regions (Figure 5d). To verify the intermingling of PDLSCs carried by the two bioinks within the final construct, we utilized distinct red and green live-cell fluorescent dyes to label the cells within the bioinks for bioprinting. After one day of culture, the fluorescence images showed a clear stratification of red and green fluorescence in the upper and lower layers, respectively. By the 7th day of culture, the images displayed an intermingling of red and green fluorescence, demonstrating the natural migration of cells across the transition area (Figure 5e).

3.3.4. ALP staining

The ALP staining results at days 7 and 14 (Figure 6a) demonstrated that PDLSCs exhibited osteogenic potential when induced. Under the stimulation of CHA, the groups cultured in PM and OM showed a higher trend of purple nodules compared to the blank control group. Notably, CHA could also partially guide the differentiation of PDLSCs toward the osteogenic lineage in a PM environment due to the presence of nHA.

3.3.5. Picro Sirius Red staining

Figure 6b illustrates the Picro Sirius Red staining results of collagen fiber secretion by PDLSCs in the control and CA-induced differentiation groups on days 1, 7, and 14. Over

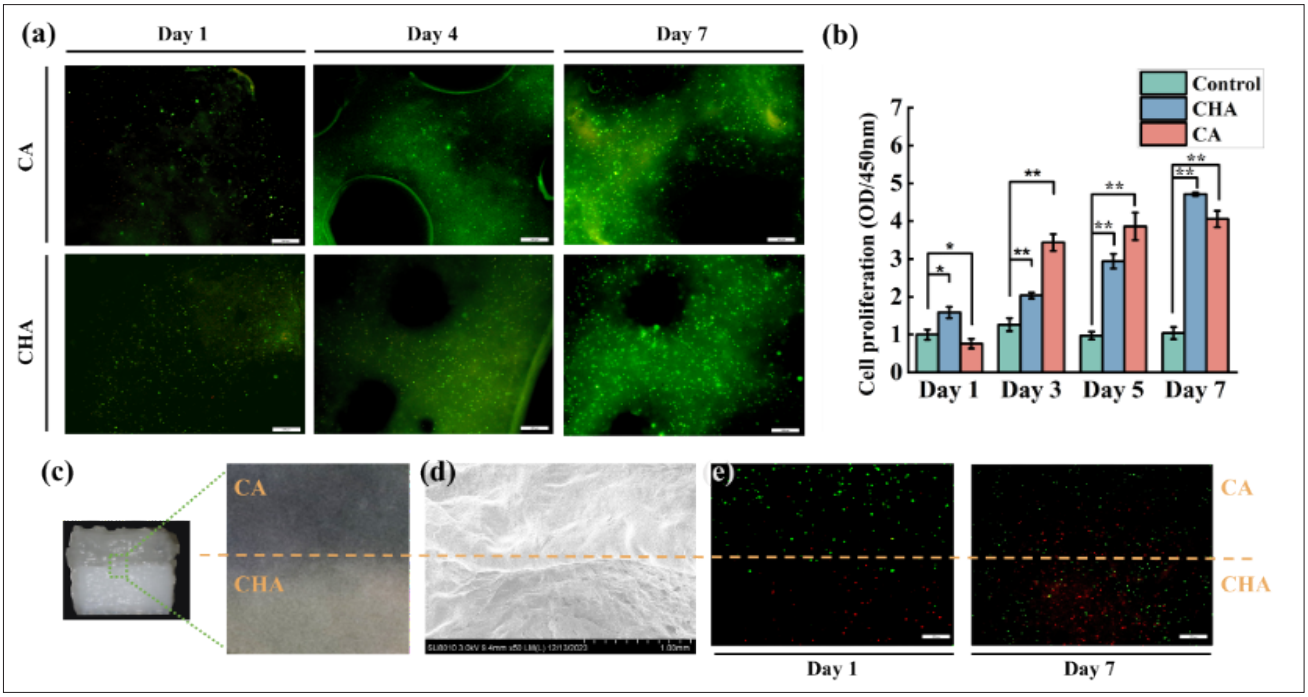

Figure 5. Cell viability and motility within the constructs. (a) Fluorescence images of live/dead staining of PDLSCs within the CA and CHA constructs at days 1, 4, and 7, with an initial cell seeding density of 1×10^6 cells/mL. (b) CCK-8 assay results for PDLSCs under the influence of CHA and CA at days 1, 3, 5, and 7 ($n = 5$). (c) Macroscopic image of the transitional structure showing an integrated and gradient variation. The upper transparent layer is composed of CA, while the lower white layer is made of CHA. (d) SEM images of the longitudinal section of the transitional structure showing an integrated result. (e) Fluorescence staining images of the longitudinal section of the transitional structure at days 1 and 7 showing the movement of cells from the upper and lower layers towards the interface over time. Cells within the bioinks of the upper and lower materials were stained with Vybrant™ DiO and Vybrant™ DiD fluorescent dyes (Thermo Scientific, USA), respectively. Scale bars: 200 μm (a, e). *$p < 0.05$; **$p < 0.01$. Abbreviations: CA: Collagen/alginate; CCK-8: Cell Counting Kit-8; CHA: Collagen/nano-hydroxyapatite/alginate; PDLSCs: Periodontal ligament stem cells; SEM: Scanning electron microscopy.

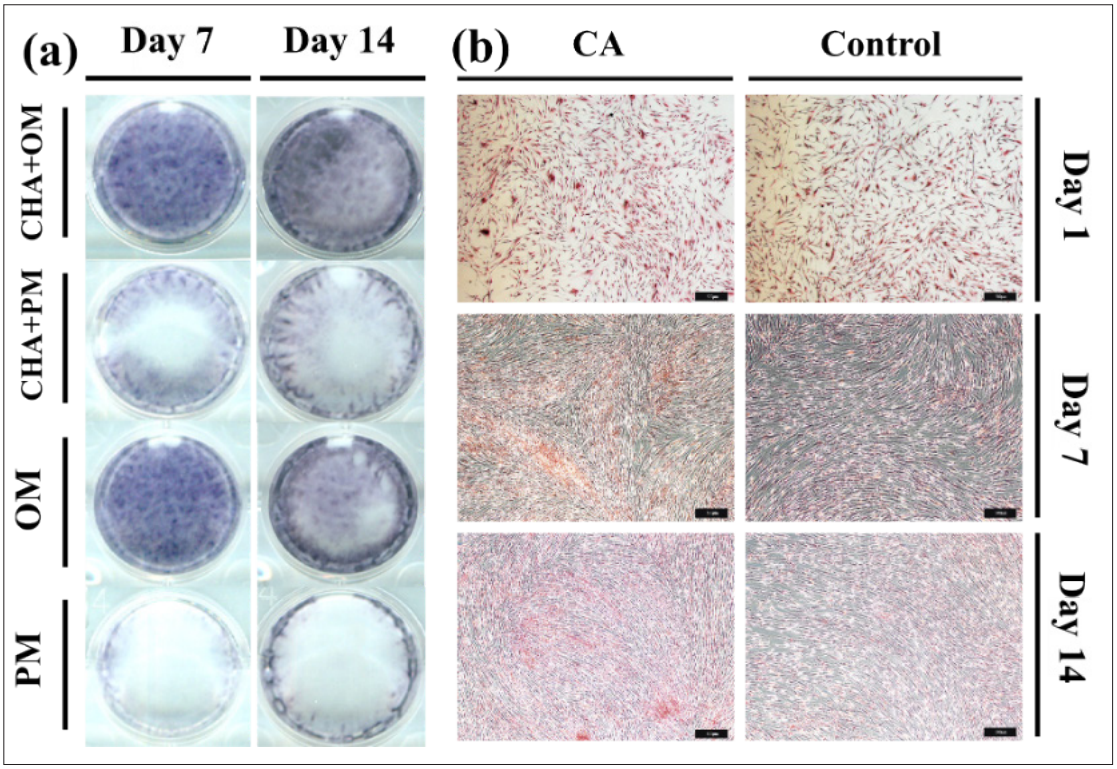

Figure 6. Differentiation staining results of PDLSCs under various material environments. (a) ALP staining results at days 7 and 14. The first row of images presents the experimental outcomes of OM cultivation under CHA material stimulation. The second row displays the results of PM cultivation under CHA material stimulation. The third row illustrates the outcomes of OM cultivation without material stimulation. The fourth row shows the results of PM cultivation without material stimulation. (b) Picro Sirius Redstaining results at days 1, 7, and 14. The images on the left column represent the experimental results under the stimulation of CA material, while the images on the right column depict the outcomes without any material stimulation. Scale bars: 500 μm. Abbreviations: CA: Collagen/alginate; CHA: Collagen/nano-hydroxyapatite/alginate; OM: osteogenic differentiation medium; PM: proliferation medium.

time, both groups displayed an increasing trend in the intensity of deep red staining, indicative of collagen fiber deposition. Comparatively, at each time point, the CA-induced differentiation group exhibited a higher amount of fibrils stained in deep red with a fuzzy appearance, while the control group demonstrated less staining and a milder effect.

3.3.6. Gene expression analysis

We employed RT-qPCR to evaluate the gene expression profiles of PDLSCs within constructs showing distinct osteogenic and fibrogenic potential, aiming to explore the influence of our fabricated constructs on the differentiation trajectory of stem cells (Figure 7). The findings indicated that under the stimulation of the CA construct, the expression levels of *COL1* and *PLAP1* were higher compared to the control group, with a slight decrease in expression over time. Additionally, the expression trends of the *FSP1* and *ELASTIN* genes exhibited an opposite trend. The *FSP1* gene expression showed an upward trend in the experimental group, while the expression of the *ELASTIN* gene progressively diminished. On day 7, when stimulated by the CHA construct, the expression level of *COL1* was higher than that of the control group; however, it declined over time. The expression of *ALP* and *RUNX2* in cells stimulated by CHA was significantly elevated compared to the control group. Furthermore, the *OPN* gene expression in cells stimulated by the CHA construct was lower and continued to decrease.

3.4. *In vivo* study

3.4.1. Histochemical analysis following ectopic transplantation in mice

Samples were harvested at weeks 2, 4, and 8 after implantation of the constructs into the dorsal region of mice. In the PDLSCs/CHA group, the remaining material's volume was significantly reduced compared to the initial volume (Figure 8c). The resorption of the material was accompanied by an increasingly evident distribution of surface blood vessels. Histological cross-sections of both constructs, stained with HE, revealed a porous meshwork, nHA nodes, and blood vessel distribution (Figure 8a and 8b). At week 2, blood vessels had infiltrated the interior of the construct. By weeks 4 and 8, the distribution of

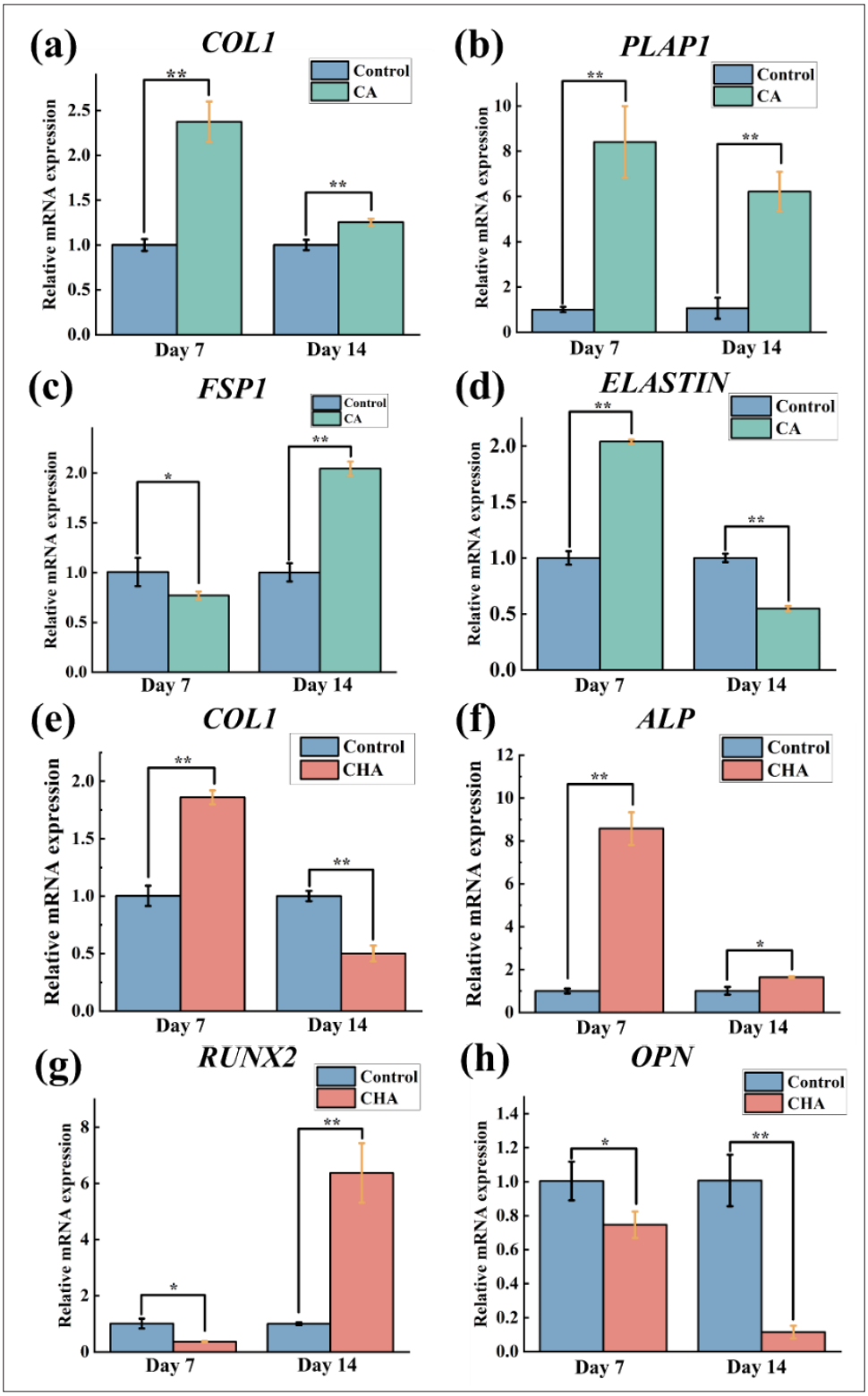

Figure 7. Gene expression in PDLSCs stimulated by different materials on days 7 and 14. (a–d) Gene expression levels of *COL1* (a), *PLAP1* (b), *FSP1* (c), and *ELASTIN* (d) in PDLSCs stimulated by CA material. (e–h) Gene expression levels of *COL1* (e), *ALP* (f), *RUNX2* (g), and *OPN* (h) in PDLSCs stimulated by CHA material. The control group represents normal PDLSCs without material stimulation. The Y-axis denotes the relative expression ratio of the target genes normalized to *GAPDH*. Data are presented as mean ± standard deviation, $n = 3$, $^{*}p < 0.05$, $^{**}p < 0.01$. Abbreviations: CA: Collagen/alginate; CHA: Collagen/nano-hydroxyapatite/alginate; PDLSCs: Periodontal ligament stem cells.

blood vessels became more profound with the increased degradation of the material. At week 8, the majority of the material had been degraded, corroborating the macroscopic findings. Compared to the cell-mixed constructs, the non-cell constructs exhibited accelerated structural degradation, while the cell-printed constructs maintained a more intact internal structure at the same time points. Masson's trichrome staining also demonstrated red-stained areas of the cell-printed constructs, suggesting the presence of mineralized extracellular matrix (ECM), whereas the non-cell constructs displayed a deep blue color, likely due to the lack of such mineralization. The semi-quantitative analysis of vascular count revealed that the number of vessels formed in the cellular constructs is consistently higher than that in the acellular constructs, and this vascular count increased over time (Figure 8d).

3.4.2. Histochemical analysis of rat tooth extraction wounds

A mouse tooth extraction model was developed to evaluate the soft tissue regenerative capacity, bone healing ability, and ARP effects of 3D constructs composed of CA/CHA, PDLSCs/CHA, and PDLSCs/CA/CHA. Micro-CT scanning was utilized to document and analyze the regenerative bone volume at the M1 extraction site. Figure 9a presents the reconstructed micro-CT images of the 4 groups (blank control, CA/CHA, PDLSCs/CHA, and PDLSCs/CA/CHA) at weeks 4 and 8 post-extraction, including 3D sagittal, 3D horizontal, and 2D frontal views of the murineM1 region. A micro-reconstruction of the central section of the extraction socket from the 3D CT images is depicted in Figure 9b, showing the healing process of the socket and the sparsity of newly formed trabecular bone (I) compared to the buccal and lingual bone plates (II). BV/TV ratio analysis was conducted according to published guidelines,[28] as shown in Figure 9c. The results indicated a significant increase in BV/TV in the material-implanted groups compared to the blank control group, with the PDLSCs/CHA/CA scaffold group showing the highest BV/TV ratio. At both weeks 4 and 8, the difference in the PDLSCs/CHA/CA scaffold group and the control group was extremely significant ($p < 0.01$). The acellular scaffold material group also demonstrated a positive trend in new bone formation compared to the control group, but the rate of bone volume increase was less than that of the cell-mixed material group.

The results suggested that the implantation of 3D constructs can effectively induce alveolar bone filling and protect the alveolar ridge post-extraction.

Histological examination of sections stained with HE and Masson's trichrome revealed that new bone formation was initiated from the apex and peripheral edges of the M1 extraction socket (Figure 10). At week 4, the absence of detectable scaffold material within the extraction socket, as indicated by the HE staining, suggested that the construct had largely degraded. In contrast to the control group without material placement, which exhibited the original morphology of the extraction socket and a small amount of woven bone, the experimental groups that received either cell-laden or non-laden layered biomaterials showed complete filling of the extraction sockets with thick trabecular bone. However, the extraction sockets implanted with non-layered material still exhibited some void structures.

To evaluate the angiogenic capacity of the tissue following the implantation of the material, we performed IHC staining for the endothelial cell marker CD31. At week 4 post-implantation, newly formed vessels were observed at the implantation sites. By week 8, the number of vessels had increased and were densely distributed within the implantation area. At week 4, the newly formed bone tissue in all groups showed strong BSP staining. By week 8, the bone tissue at both the control and implantation sites exhibited mild to moderate BSP staining. Positive expression of OPN was detected in osteoblasts and osteocytes surrounding and within the newly formed trabecular bone, with the most pronounced expression in the control group. The expression of OPN was significantly lower at week 8 compared to at week 4. COL-1 and COL-3 were uniformly expressed in both bone and soft tissues. The expression of CTGF showed an increasing trend with the progression of healing time.

Compared to the acellular material group, the material group containing PDLSCs exhibited significantly deeper staining of the osteogenic marker BSP at 4 weeks post-extraction, along with more intense staining of the vascular marker CD31. The same trend was observed in the IHC of soft tissue markers COL-1, CTGF, and COL-3. The PDLSCs/CA/CHA material group demonstrated higher expression levels of vascular, bone, and soft tissue markers early post-extraction, as evidenced by the IHC results when compared to the other material groups (Figure 11).

We employed a semi-quantitative approach to compare the expression levels of markers (Figure 12a–h). The CD31 expression in the implanted material group was higher than that in the control group. The experimental group exhibited a decreasing trend in BSP and OPN expression. Compared to the control group, the CTGF expression in the experimental group remained consistently higher. In both bone and superficial soft tissues, the expression of COL-1 in the experimental group was consistently higher than in the control group, while the content of COL-3 in the experimental group decreased over time compared to

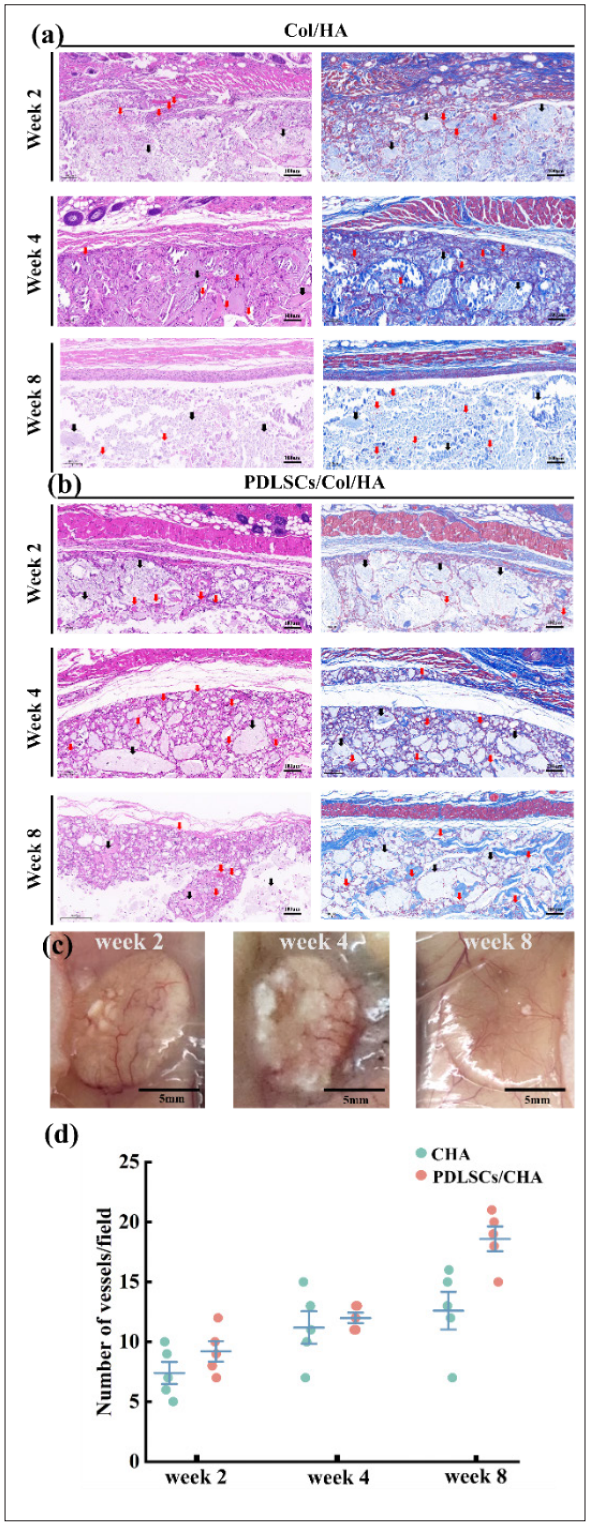

Figure 8. Ectopic implantation of acellular and cellular constructs on the dorsal region of mice followed by sample collection at weeks 2, 4, and 8 post-implantation. (a) Histological sections of acellular CHA constructs harvested at weeks 2, 4, and 8, stained with HE and Masson's trichrome. Scale bar: 100 μm. (b) Histological sections of cellular CHA constructs harvested at the same time points, stained with HE and Masson's trichrome. Scale bar: 100 μm. The red arrows indicate blood vessels and the blue arrows indicate the material. (c) Macroscopic photographs of the cellular CHA constructs at weeks 2, 4, and 8. Scale bar: 5 mm. (d) Semi-quantitative analysis of vascular density. $^{*}p < 0.05$, $^{**}p < 0.01$. Abbreviations: CA: Collagen/alginate; CHA: Collagen/nano-hydroxyapatite/alginate; Col: Collagen; HE: Hematoxylin and eosin; PDLSCs: Periodontal ligament stem cells.

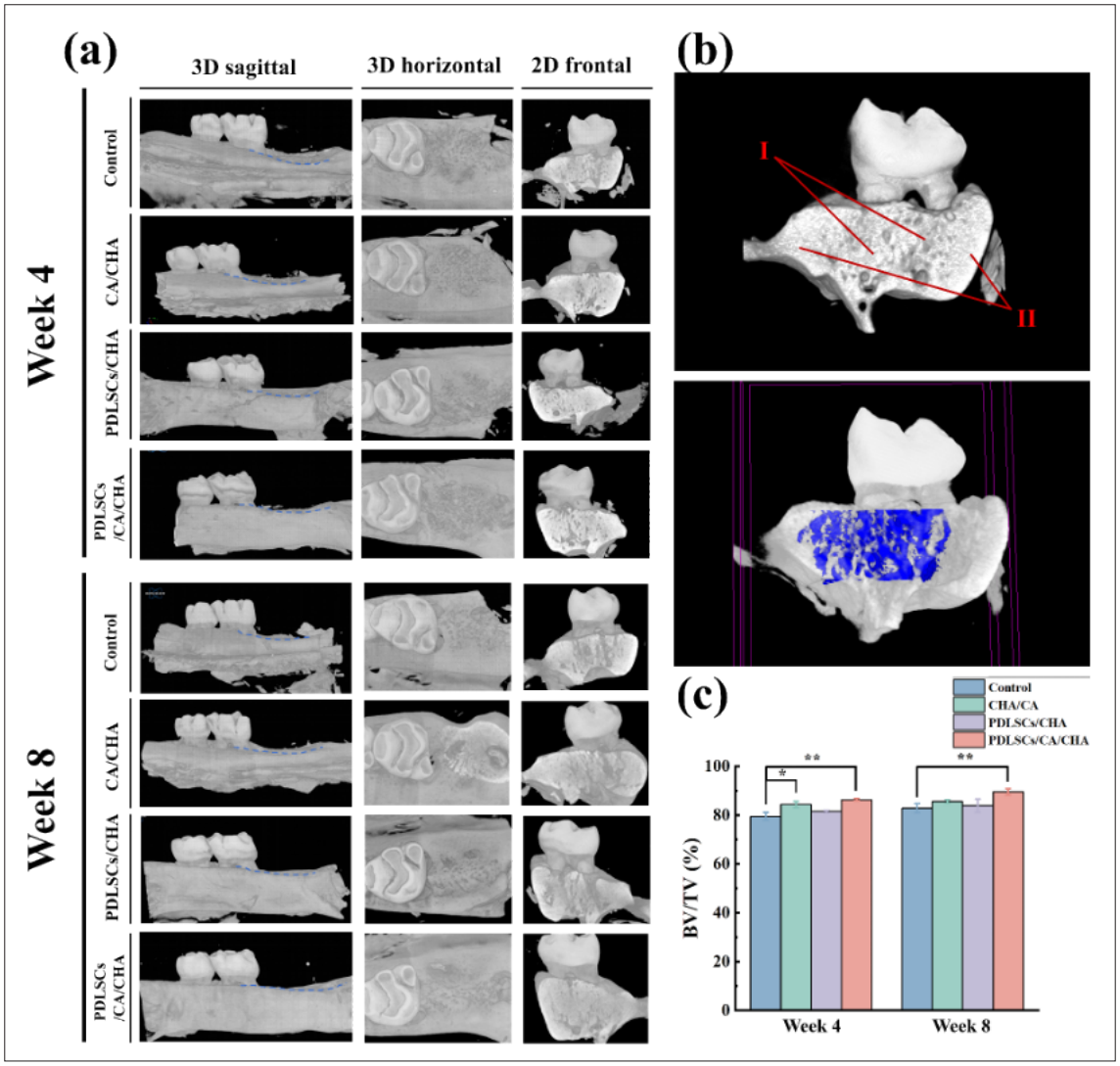

Figure 9. Bone tissue regeneration at the extraction site in rats. (a) The reconstructed micro-CT images of the M1 region in mice at 4 and 8 weeks post-extraction presented in 3D sagittal, 3D horizontal, and 2D frontal views. The blue dashed line delineates the resorption of buccal bone. At each time point (weeks 4 and 8), the first row of images shows the results of extraction sockets in the control group without any material implantation. The second row displays the outcomes of extraction sockets implanted with acellular CA/CHA materials. The third row presents the results of extraction sockets implanted with PDLSCs/CHA non-layered materials. The fourth row illustrates the outcomes of extraction sockets implanted with PDLSCs/CA/CHA materials. (b) Microscopic reconstruction process of the central portion of the rat extraction socket, with newly formed bone indicated by blue shading. The red arrow points to the newly formed bone (I) and the buccal and lingual bone plates (II). (c) Quantitative analysis of BV/TV within the murine extraction sockets. $^{*}p < 0.05$, $^{**}p < 0.01$. Abbreviations: BV/TV: Bone volume-to-tissue volume ratio; CA: Collagen/alginate; CHA: Collagen/nano-hydroxyapatite/alginate; micro-CT: Micro-computed tomography; PDLSCs: Periodontal ligament stem cells.

the control group. To investigate the quality of the formed soft tissue fibers, we calculated the ratio of COL-1 to COL-3 in soft tissue (Figure 12i). The results indicated that the ratio in the control group was significantly lower than in the implanted material group, with the stratified material group showing the highest ratio. To investigate the impact of the nHA content variation within the material on the formation of new bone, we also analyzed the difference in BSP expression between the denser bone areas on the surface and the internal trabecular bone regions. In the same sample, compared to the internal newly formed trabeculae, the surface denser newly formed bone material exhibited higher BSP expression. After implantation with the stratified material, the content of BSP in the bone was consistently higher than that in the non-stratified material implant. The trend of change over time was similar to that observed in the total newly formed bone as previously described (Figure 12g).

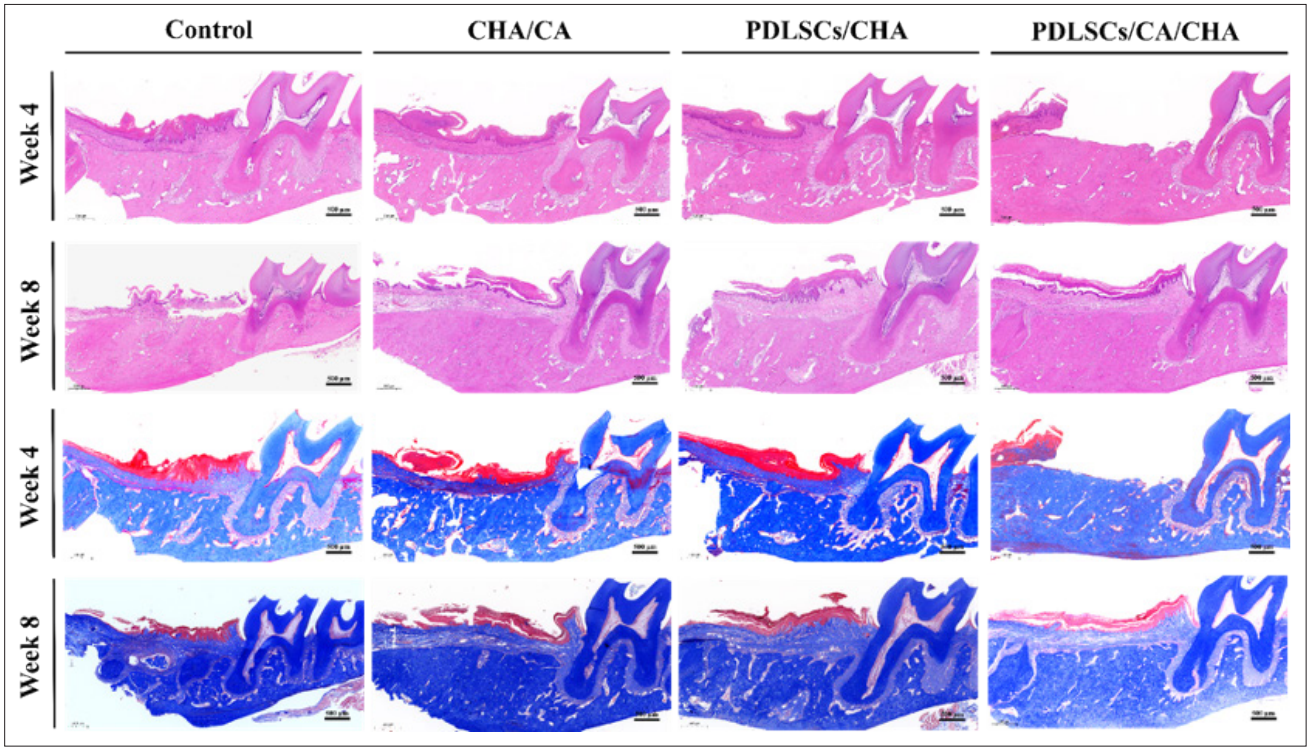

Figure 10. Histological sections of rat extraction sockets, obtained from longitudinal cuts, were stained with HE and Masson's trichrome. Scale bar: 500 μm. Abbreviations: CA: Collagen/alginate; CHA: Collagen/nano-hydroxyapatite/alginate; HE: Hematoxylin and eosin; PDLSCs: Periodontal ligament stem cells.

4. Discussion

In this research, we developed a 3D construct featuring a gradient in concentration, integration, and heterologous differentiation of one kind of stem cells, aimed at fostering the regeneration of both hard and soft tissues. This innovative approach to ARP has been validated through *in vitro* cellular assays and *in vivo* animal experiments, demonstrating its potential for further clinical investigation in the simultaneous regeneration of hard and soft tissues.

Hydrogel bioinks provide a 3D microenvironment for cells that closely mimics the ECM, exhibiting excellent biocompatibility. Collagen within the bioink offers attachment sites for cells, thereby promoting cell proliferation and differentiation.[31] However, the relatively low mechanical properties of collagen can limit its utility for subsequent *in vitro* and *in vivo* studies.[32] This study incorporated collagen with nHA to encapsulate stem cells within the hydrogel bioink and employed 3D bioprinting technology to construct scaffolds. The test results indicate that the hydrogel-based bioinks formulated with CA and CHA exhibit shear-thinning properties, which prevent excessive shear stress from affecting cell viability during the printing process.[33] Rheological frequency sweep measurements revealed that both ink solutions demonstrate gel-like characteristics, enabling them to be extruded from the nozzle. This suggests that gelation occurs uniformly and allows for more controlled ink deposition. Collagen provides tensile strength to the skeletal structure, while dispersed nHA crystals contribute to compressive strength.[34] Our physicochemical analysis of the bioink in this study corroborated these findings. The mechanical properties of the stratified CHA/CA construct aligned with the observed elasticity range of oral soft tissues, which, akin to natural skin, span from 10 to 100 kPa.[35]

3D bioprinting uses computer-aided design to engineer intricate structures, layering bioinks containing cells and biomaterials to create complex, 3D living constructs. This technology allows for the precise deposition of cell-laden biomaterials, facilitating the construction of complex 3D architectures. It has widespread application in the field of tissue regeneration.[36] During the printing process, the scaffold's material composition can be controlled by varying the porosity and geometric configuration of the structure.

As previously mentioned, to mimic the natural variation in human bone HA content, the scaffolds were designed with different pore sizes and densities in the upper and lower layers, thereby varying the nHA content.

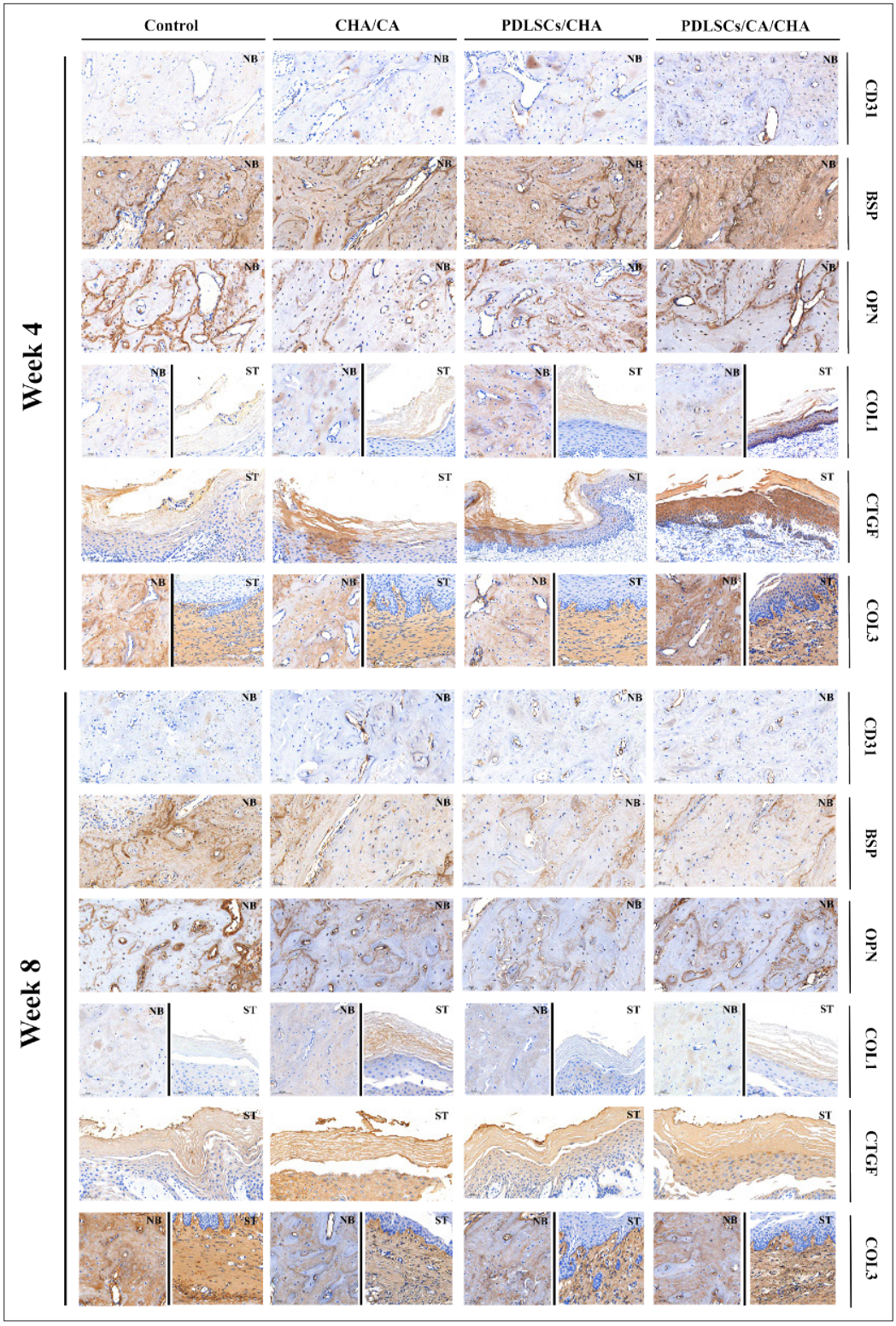

Figure 11. IHC results of longitudinal sections from murineextraction socket samples. The images from the first to the sixth rows depict the IHC results for CD31, BSP, OPN, COL-1, CTGF, and COL-3, respectively. The left four columns and the right four columns display the immunostaining results for each group at weeks 4 and 8, respectively. Scale bar: 50 μm. Abbreviations: CA: Collagen/alginate; CHA: Collagen/nano-hydroxyapatite/alginate; IHC: Immunohistochemistry; NB: New bone; PDLSCs: Periodontal ligament stem cells; ST: Soft tissue.

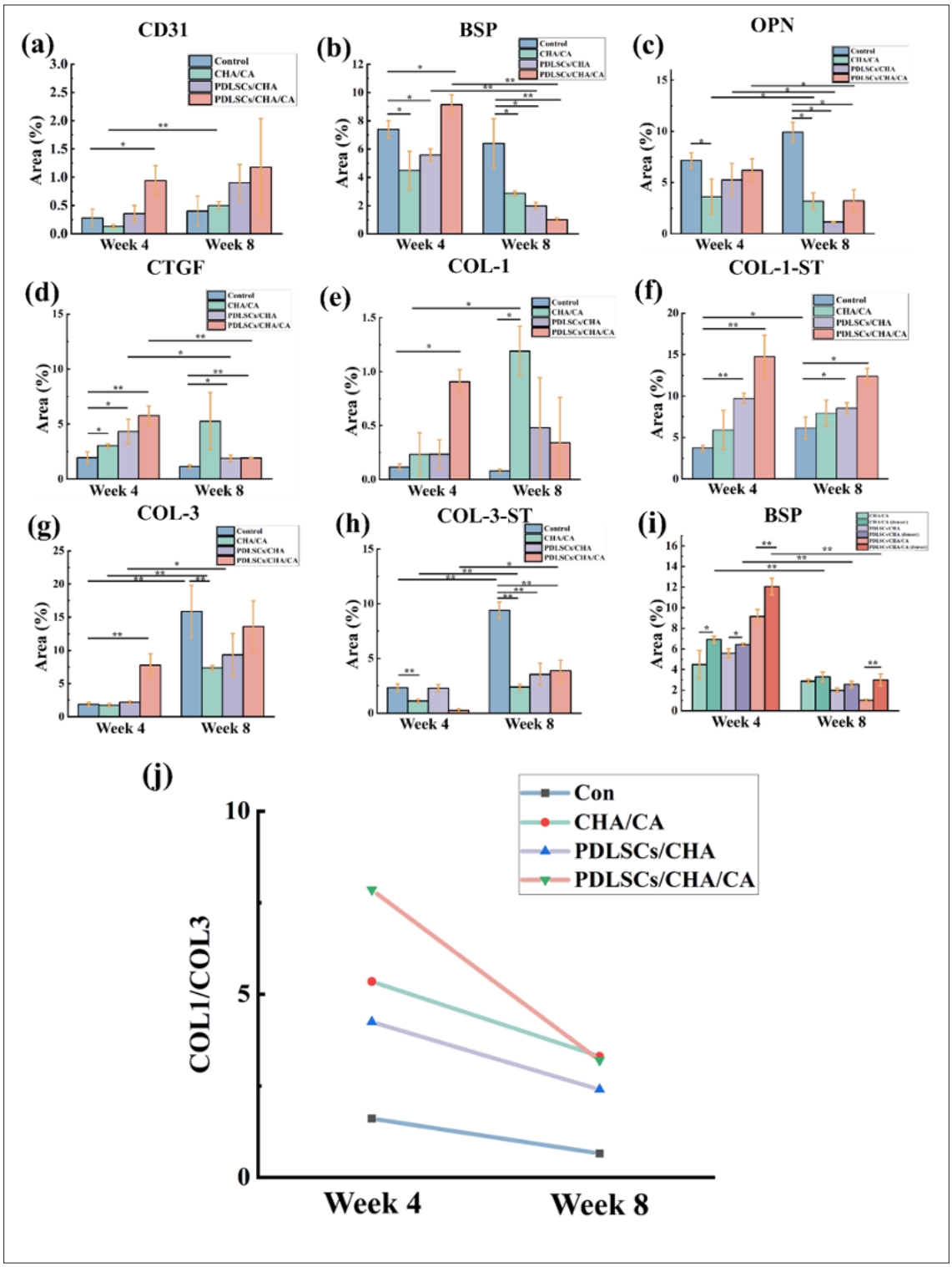

Figure 12. IHC expression level results. (a–h) IHC-based expression levels of markers in the longitudinal sections of murine tooth socket samples: CD31 (a), BSP (b), OPN (c), CTGF (d), COL-1 (e), COL-1-ST (f), COL-3 (g), and COL-3-ST (h). The results are presented as semi-quantitative data. (i) Semi-quantitative results of BSP expression in the internal bone and the denser superficial bone layer. (j) The ratio of COL-1 to COL-3. *$p < 0.05$, **$p < 0.01$. Abbreviations: CA: Collagen/alginate; CHA: Collagen/nano-hydroxyapatite/alginate; IHC: Immunohistochemistry; PDLSCs: Periodontal ligament stem cells; ST: Soft tissue.

The upper portion of the CHA component was designed with a denser internal lattice, while the lower portion had a sparser lattice, to control the nHA concentration. Thus, by designing the internal lattice space of the 3D construct, we created an integrated repair structure with gradient variations.

The SEM results showed that macro-lattice and micro-porosity within these scaffolds are considered crucial for tissue regeneration.[37] Research indicated that successful vascularization of engineered tissues *in vivo* requires space within the scaffold (>200 μm) to facilitate host cell infiltration and subsequent angiogenesis.[38] The porous structure of the material can promote cell infiltration, microvasculature formation, and enhance cell survival and differentiation potential.[39] Additionally, 150–700 μm porous biomaterials can enhance osteoconduction, facilitating the integration of the scaffold with host bone.[40] Researches also revealed that the porosity of the micropores (<10 μm) plays a significant role in enhancing the osteoinductive properties of the scaffold.[41,42] The presence of micropores enhances the permeability of the scaffold, thereby providing more sites for protein adsorption and facilitating its degradation.[43] This aligns with the structure of our material, which features a lattice of large pores (450–600 μm) and a surface with microporous structures, resembling those of scaffolds created by other researchers that exhibit osteoconductivity and good biocompatibility.

In this study, PDLSCs were subjected to flow cytometry to assess their phenotype. The results indicated that these cells exhibited characteristics of MSCs with multipotent differentiation capabilities. Research by Liu et al.[44] has demonstrated the trilineage differentiation potential of PDLSCs into osteoblasts, fibroblasts, and cementoblasts.[16] Studies have also shown that hydrogels composed of collagen and nHA enhance the osteogenic differentiation potential of MSCs. Togo et al.[45] discovered that embryonic stem cells can differentiate into fibroblast-like cells within 3D type I collagen gels,[46] and research suggested that the alignment of collagen matrices can influence the differentiation of fibroblasts. Consequently, this study encapsulated PDLSCs within hydrogels of varying compositions to guide their differentiation toward fibroblastic and osteogenic lineages, aiming to achieve simultaneous regeneration of hard and soft tissues.

Live/dead staining demonstrated that cell viability increased progressively with extended post-printing culture durations. The CCK-8 assay results indicated that material stimulation could promote cell proliferation. Within the initial 5 days post-printing, cells under CHA stimulation did not proliferate as extensively as those under CA stimulation. This observation may correlate with other studies reporting that an increase in amorphous calcium phosphate can potentially induce some cell apoptosis.[47]

PDLSCs cultured in a regular medium without osteogenic supplements showed no inclination toward osteogenic differentiation. However, upon the addition of CHA material stimulation, PDLSCs in regular culture conditions also exhibited a certain degree of osteogenic tendency. Additionally, the results demonstrated the potential of PDLSCs to differentiate into cells of both osteogenic and fibroblastic lineages under material stimulation during *in vitro* differentiation assays. Furthermore, the gene analysis test confirmed the differentiation trend of these cells. Under the stimulation of CA material, the expression levels of *COL1*, *PLAP1*, and *ELASTIN* in PDLSCs were significantly higher compared to the control group on day 7 ($p < 0.01$). Additionally, *FSP1* expression was double that of the control group on day 14. COL-1, a crucial component of the soft tissue collagen fibrils, contributes to the tensile strength of the ECM associated with tendons or ligaments.[48] In research by Takedachi et al.[49] *PLAP1* maintains the soft tissue characteristics of the periodontal tissue and plays a vital role in maintaining the homeostasis of periodontal tissue under mechanical stress. *FSP1* expression is a prominent indicator of fibroblastic differentiation.[50] Elastin, an essential ECM protein required for maintaining the elastic properties of skin, plays a significant role in the wound healing process.[51] Therefore, the gene expression results confirmed that CA material stimulation favored the differentiation of PDLSCs toward soft tissue lineage.

Concurrently, under CHA stimulation, PDLSCs differentiated toward the osteogenic lineage. On day 7, the expression levels of osteogenic factors *ALP*in the experimental group were higher than in the control group. *ALP* is a distinctive biochemical marker of the bone formation process[52] On day 14, the expression of *ALP* was 1.5 times higher than in the control group, indicating better osteogenic differentiation of PDLSCs in the experimental group ($p < 0.05$). The expression of *RUNX2* was slightly lower than in the control group on day 7, but by day 14, it showed a significant increase compared to the control group, further demonstrating the osteogenic induction capability of the material.

In this study, we employed murineheterotopic transplantation and tooth extraction wound healing experiments to validate the biocompatibility and the simultaneous regeneration capabilities of both hard and soft tissues of the material. Macroscopic observation of the tissue samples from the mouse back revealed the ingrowth of blood vessels and the degree of *in vivo* degradation of the material. Following the implantation of cell-printed

constructs, we observed more intact structures, which may be related to the encapsulation of cells within the constructs.[53,54]

The use of 3D porous scaffold materials for ARP remains an advanced tissue engineering technique. We innovatively introduced PDLSCs and promoted their bidirectional differentiation into bone and soft tissues within the scaffold material. At week 4 post-surgery, the extraction socket site in the control group still displayed empty socket structures, whereas new bone formation without residual scaffold material was observable in the histological sections of the experimental group's murine alveolar sockets. A previous study has indicated that rapid material degradation promotes the formation of new bone.[55] This conclusion is also supported by the 3D computed tomography (CT) images and BV/TV data of rats. It is noteworthy that the volume of BV in the stratified scaffold materials with or without cells was greater than that in the non-stratified implant materials. This may be attributed to the altered content of HA in the upper and lower layers of the CHA material.

Subsequently, we performed IHC staining for various markers to evaluate the specific changes in tissue at the implant site. Angiogenesis plays a crucial role in the wound healing process, providing oxygen and nutrients from the local vascular system to support tissue regeneration.[38] Through CD31 staining, we demonstrated that the implanted material did not hinder the normal process of blood clotting but instead increasedthevascular distribution over time, leading tomoreabundant and denser vascular networks. One study has demonstrated a successful attempt at seeding endothelial cells onto porous scaffolds prior to implantation to expedite vascular formation.[56] This could explain the significant increase in vascular distribution observed after the incorporation of stem cells, as indicated by staining results. BSP is a non-collagenous ECM protein associated with mineralized tissues and is related to the formation of alveolar bone and cementum. It is a marker protein for osteoblast differentiation.[57,58] The IHC results of this study showed stronger BSP staining in the newly formed bone during the early stages of healing, with staining intensity diminishing as the bone matures, consistent with other findings.[58] Additionally, Candeliere et al.[59] investigated the expression levels of BSP in the superficial and internal bones of the skull, revealing higher concentrations in the superficial areas. In our IHC semi-quantitative analysis, we validated the findings for the implanted material groups, observing similar results. We discovered that the superficial bone in the group implanted with stratified material exhibited higher BSP content compared to the non-stratified material group. This may be attributed to the stratified material's ability to facilitate a more natural gradient of bone regeneration, which is superior to that of the non-stratified material. In line with the results of the aforementioned PCR experiments, the staining results for OPN in the implanted material group were lighter than in the control group, and the expression of OPN in the sections at week 8 was lower than at week 4, indicating that the formed bone is maturing. This is similar to the findings of Chen et al.[60] Therefore, the staining results for bone matrix proteins suggested that the new bone matured more quickly after the implantation of the material, bringing the potential for the effectiveness of subsequent implant restoration. Type I collagen and type III collagen are the primary constituents of collagen fibers within the ECM. They exhibit distinct distribution patterns, with type I collagen showing a strong, diffused presence in both soft and hard tissue matrices of the control and material groups. Although type I collagen is generally recognized as more mature and possessing superior mechanical properties, type III collagen is typically observed earlier in the woundhealing phase. *In vitro* studies by Xin et al.[61] found a higher ratio of COL-1 to COL-3, signifying a better quality formation of collagen fibers and implying a more mature structure. Our *in vivo* experimental results demonstrated that, at week 8, the staining for COL-1 was weaker in the control group compared to the material group, while the staining for COL-3 was stronger in the control group than in the material group. This could indicate that the newly formed soft tissue at the implant site possesses superior mechanical properties due to the composition of the implanted materials, especially in the PDLSCs/CHA/CA experimental group. CTGF is considered to play a role in angiogenesis during wound healing after tooth extraction, with migrating and proliferating endothelial cells in granulation tissue expressing high levels of CTGF.[62] This suggests that CTGF may contribute to facilitating wound healing by initiating angiogenesis and granulation tissue formation. IHC results from our experiments showed a higher expression of CTGF in the material group compared to the control group. Collectively, these findings indicated that, as compared to the control group, the implanted stratified material effectively promoted the regeneration of both hard tissue in the alveolar socket and the overlying soft tissue following tooth extraction. Notably, the inclusion of mixed cells notably enhanced the tissue regenerative outcomes.

Preliminary findings of our research indicated that the integrated 3D constructs, which are characterized by variations in concentration, use of CA and CHA, and also integrated with PDLSCs, underscored the need to introduce innovative therapeutic strategies for the conservation of both oral soft and hard tissues. Previous studies have demonstrated that biomaterials utilized in

traditional ARP reduce the amount of newly formed bone and may impede the healing process of the alveolar socket.[63,64] In this research, we employed a murine model, which shows distinct healing patterns following tooth extraction compared to humans. To further substantiate the efficacy of the composite constructs and to confirm their capacity to facilitate rapid alveolar bone healing, subsequent experiments will be extended to large animal models, such as the beagle dogs. To surmount the clinical challenges faced in obtaining patient-derived stem cells for the present study, we intentionally included a cell-free group in the *in vivo* experiments. It is noteworthy that while the outcome did not match the performance of the groups incorporating stem cells, the cell-free constructs still managed to achieve commendable regenerative results in comparison to the control groups, indicating their potential utility in regenerative therapy.

5. Conclusion

Made of CA and CHA bioinks, a 3D layered construct featuring gradual variations in HA concentration was ingeniously engineered via bioprinting in this study for the integrated repair of tissues during ARP. This innovative process involves not only the incorporation of PDLSCs and the enhancement of scaffold's viability, but also the stimulation of their heterotopic differentiation ability. Applying this construct to all transplantation and post-tooth extraction in a murine model demonstrated its biocompatibility and its capacity to enhance the integrated regeneration of oral hard and soft tissues. This sophisticated construct may pave the way for practical use as customized integrated material following tooth extraction, showcasing the potential for clinical translation.

Acknowledgments

None.

Funding

This work was supported by the National Key Research and Development Program of China (2017YFA0701302, PKUSS20200113).

Conflict of interest

The authors declare they have no competing interests.

Author contributions

Conceptualization: Zhihui Tang, Qing Li
Formal analysis: Huilin Zhu, Ke Yi
Investigation: Huilin Zhu, Ke Yi
Methodology: Huilin Zhu
Writing–original draft: Huilin Zhu
Writing–review & editing: Zhihui Tang, Qing Li

Ethics approval and consent to participate

Isolation of primary human PDLSCs was approved by the Ethics Committee of the Peking University School and Hospital of Stomatology (PKUSSIRB-201950166), with informed consent obtained from all subjects or their legal guardians. Animal experiments of this study were approved by the Laboratory Animal Research Ethics Committee of Peking University Health Science Center (Approval No.: DLASBD0054).

Consent for publication

Not applicable.

Availability of data

Data is available from the corresponding author upon reasonable request.

Supplemental information

Video S1. Visual demonstration video of the mechanical properties of the construct.

References

1. Tan WL, Wong TLT, Wong MCM, Lang NP. A systematic review of post-extractional alveolar hard and soft tissue dimensional changes in humans. *Clin Oral Implants Res.* 2012;23(S5):1-21.
doi: 10.1111/j.1600-0501.2011.02375.x.

2. Khzam N, Arora H, Kim P, Fisher A, Mattheos N, Ivanovski S. Systematic review of soft tissue alterations and esthetic outcomes following immediate implant placement and restoration of single implants in the anterior maxilla. *J Periodontol.* 2015;86(12):1321-1330.
doi: 10.1902/jop.2015.150287.

3. Farmer M, Darby I. Ridge dimensional changes following single-tooth extraction in the aesthetic zone. *Clin Oral Implants Res*. 2014;25(2):272-277.
doi: 10.1111/clr.12108.

4. Aribau-Gumà C, Jorba-García A, Sánchez-Torres A, Sànchez-Garcés M. Alveolar ridge preservation: an overview of systematic reviews. *Int J Oral Maxillofac Surg.* 2022;51(2):234-242.
doi: 10.1016/j.ijom.2021.06.002.

5. Barootchi S, Tavelli L, Majzoub J, Stefanini M, Wang HL, Avila-Ortiz G. Alveolar ridge preservation: complications and cost-effectiveness. *Periodontol* 2000. 2023;92(1): 235-262.
doi: 10.1111/prd.12469.

6. Montazerian H, Davoodi E, Baidya A, Baghdasarian S, Sarikhani E, Meyer CE, Haghniaz R, Badv M, Annabi N, Khademhosseini A, Weiss PS. Engineered Hemostatic Biomaterials for Sealing Wounds. *Chem Rev* 2022;122(15):12864-12903. doi: 10.1021/acs.chemrev.1c01015.

7. Ayari H. The use of periodontal membranes in the field of periodontology: spotlight on collagen membranes. *J Appl Biomed* 2022;20(4):154-162. doi: 10.32725/jab.2022.020.

8. Canullo L, Pesce P, Antonacci D, Ravidà A, Galli M, Khijmatgar S, Tommasato G, Sculean A, Del Fabbro M. Soft tissue dimensional changes after alveolar ridge preservation using different sealing materials: a systematic review and network meta-analysis. *Clin Oral Investig*. 2022;26(1): 13-39. doi: 10.1007/s00784-021-04192-0.

9. Abere DV, Ojo SA, Oyatogun GM, Paredes-Epinosa MB, Niluxsshun MCD, Hakami A. Mechanical and morphological characterization of nano-hydroxyapatite (nHA) for bone regeneration: a mini review. *Biomed Eng Adv* 2022;4(3):100056. doi: 10.1016/j.bea.2022.100056.

10. Rosa N, Moura MFSF, Olhero S, Simoes R, Magalhães FD, Marques AT, Ferreira JPS, Reis AR, Carvalho M, Parente M. Bone: an outstanding composite material. *Appl Sci* 2022;12(7):1-16. doi: 10.3390/app12073381.

11. Han HS, Lee JT, Oh S, Cho YD, Kim S. Effectiveness of a collagen matrix seal and xenograft in alveolar ridge preservation: an experimental study in dogs. *Sci Rep* 2024;14(1):1-10. doi: 10.1038/s41598-023-50370-3.

12. Gabay E, Katorza A, Zigdon-Giladi H, Horwitz J, Machtei EE. Histological and dimensional changes of the alveolar ridge following tooth extraction when using collagen matrix and collagen-embedded xenogenic bone substitute: a randomized clinical trial. *Clin Implant Dent Relat Res.* 2022;24(3):382-390. doi: 10.1111/cid.13085.

13. Tonar Z, Khadang I, Fiala P, Nedorost L, Kochová P. Quantification of compact bone microporosities in the basal and alveolar portions of the human mandible using osteocyte lacunar density and area fraction of vascular canals. *Ann Anat*. 2011;193(3):211-219. doi: 10.1016/j.aanat.2011.02.001.

14. Reznikov N, Shahar R, Weiner S. Bone hierarchical structure in three dimensions. *Acta Biomater.* 2014;10(9):3815-3826. doi: 10.1016/j.actbio.2014.05.024.

15. Bartold PM. Connective tissues of the periodontium--preface. *Periodontol*. 2000. 2000;24(1):7-8. doi: 10.1034/j.1600-0757.2000.2240101.x.

16. Liu J, Zhao Z, Ruan J, Weir MD, Ma T, Ren K, Schneider A, Oates TW, Li A, Zhao L, Xu HHK. Stem cells in the periodontal ligament differentiated into osteogenic, fibrogenic and cementogenic lineages for the regeneration of the periodontal complex. *J Dent*. 2020;92:103259. doi: 10.1016/j.jdent.2019.103259.

17. Seo BM, Miura M, Gronthos S, Bartold PM, Batouli S, Brahim J, Young M, Robey PG, Wang CY, Shi S. Investigation of multipotent postnatal stem cells from human periodontal ligament. *Lancet*. 2004;364(9429):149-155. doi: 10.1016/S0140-6736(04)16627-0.

18. Li M, Sun L, Liu Z, Shen Z, Cao Y, Han L, Sang S, Wang J. 3D bioprinting of heterogeneous tissue-engineered skin containing human dermal fibroblasts and keratinocytes. *Biomater Sci*. 2023;11(7):2461-2477. doi: 10.1039/d2bm02092k.

19. Jian H, Li X, Dong Q, Tian S, Bai S. In vitro construction of liver organoids with biomimetic lobule structure by a multicellular 3D bioprinting strategy. *Cell Prolif.* 56(5):1-9. doi: 10.1111/cpr.13465.

20. Dai W, Zhang L, Yu Y, Yan W, Zhao F, Fan Y, Cao C, Cai Q, Hu X, Ao Y. 3D Bioprinting of heterogeneous constructs providing tissue-specific microenvironment based on host–guest modulated dynamic hydrogel bioink for osteochondral regeneration. *Adv Funct Mater*. 2022;32(23):1-12. doi: 10.1002/adfm.202200710.

21. Zhang Y, Li D, Liu Y, Peng L, Lu D, Wang P, Ke D, Yang H, Zhu X, Ruan C. 3D-bioprinted anisotropic bicellular living hydrogels boost osteochondral regeneration via reconstruction of cartilage–bone interface. *Innovation*. 2024;5(1):100542. doi: 10.1016/j.xinn.2023.100542.

22. Nguyen LH, Kudva AK, Guckert NL, Linse KD, Roy K. Unique biomaterial compositions direct bone marrow stem cells into specific chondrocytic phenotypes corresponding to the various zones of articular cartilage. *Biomaterials*. 2011;32(5):1327-1338. doi: 10.1016/j.biomaterials.2010.10.009.

23. Balestri W, Hickman GK, Morris RH, Hunt JA, Reinwald Y. Triphasic 3D in vitro model of bone-tendon-muscle interfaces to study their regeneration. *Cells*. 2023; 12(2):313. doi: 10.3390/cells12020313.

24. Panduwawala CP, Zhan X, Dissanayaka WL, Samaranayake LP, Jin L, Zhang C. In vivo periodontal tissue regeneration by periodontal ligament stem cells and endothelial cells in three-dimensional cell sheet constructs. *J Periodontal Res.* 2017;52(3):408-418. doi: 10.1111/jre.12405.

25. Zhu Y, Wang W, Chen Q, Ren T, Yang J, Li G, Qi Y, Yuan C, Wang P. Bioprinted PDLSCs with high-concentration GelMA hydrogels exhibit enhanced osteogenic differentiation in

vitro and promote bone regeneration in vivo. *Clin Oral Investig*. 2023;27(9):5153-5170.
doi: 10.1007/s00784-023-05135-7.

26. Adolpho LF, Lopes HB, Freitas GP, Weffort D, Campos Totoli GG, Loyola Barbosa AC, Freire Assis RI, Silverio Ruiz KG, Andia DC, Rosa AL, Beloti MM. Human periodontal ligament stem cells with distinct osteogenic potential induce bone formation in rat calvaria defects. *Regen Med*. 2022;17(6):341-353.
doi: 10.2217/rme-2021-0178.

27. Chen J, Ahmad R, Li W, Swain M, Li Q. Biomechanics of oral mucosa. *J R Soc Interface*. 2015;12(109):20150325.
doi: 10.1098/rsif.2015.0325.

28. Bouxsein ML, Boyd SK, Christiansen BA, Guldberg RE, Jepsen KJ, Müller R. Guidelines for assessment of bone microstructure in rodents using micro-computed tomography. *J Bone Miner Res*. 2010;25(7):1468-1486.
doi: 10.1002/jbmr.141.

29. Boularaoui S, Shanti A, Khan KA, Iacoponi S, Christoforou N, Stefanini C. Harnessing shear stress preconditioning to improve cell viability in 3D post-printed biostructures using extrusion bioprinting. *Bioprinting*. 2022;25(8):e00184.
doi: 10.1016/j.bprint.2021.e00184.

30. Popescu F, Titorencu I, Albu Kaya M, Miculescu F, Tutuianu R, Coman AE, Danila E, Marin MM, Ancuta DL, Coman C, Barbilian A. Development of innovative biocomposites with collagen, keratin and hydroxyapatite for bone tissue engineering. *Biomimetics*. 2024;9(7):428.
doi: 10.3390/biomimetics9070428.

31. Elango J, Hou C, Bao B, Wang S, Maté Sánchez de Val JE, Wenhui W. The molecular interaction of collagen with cell receptors for biological function. *Polymers (Basel)*. 2022;14(5):1-25.
doi: 10.3390/polym14050876.

32. Bose S, Li S, Mele E, Silberschmidt VV. Exploring the mechanical properties and performance of type-I collagen at various length scales: a progress report. *Materials (Basel)*. 2022;15(8):1-17.
doi: 10.3390/ma15082753.

33. Schwab A, Levato R, D'Este M, Piluso S, Eglin D, Malda J. Printability and shape fidelity of bioinks in 3D bioprinting. *Chem Rev*. 2020;120(19):11028-11055.
doi: 10.1021/acs.chemrev.0c00084.

34. Clarke B. Normal bone anatomy and physiology. *Clin J Am Soc Nephrol*. 2008;3(Suppl 3):S131-S139.
doi: 10.2215/CJN.04151206.

35. Joodaki H, Panzer MB, Skin mechanical properties and modeling: a review. *Proc Inst Mech Eng H*. 2018;232(4):323-343.
doi: 10.1177/0954411918759801.

36. P Jain, H Kathuria, N Dubey. Advances in 3D bioprinting of tissues/organs for regenerative medicine and in-vitro models. *Biomaterials*. 2022;287(8):121639.
doi: 10.1016/j.biomaterials.2022.121639.

37. Ghayor C, Bhattacharya I, Guerrero J, Ozcan M, Weber FE. 3D-printed HA-based scaffolds for bone regeneration: microporosity, osteoconduction and osteoclastic resorption. *Materials*. 2022;15(4):1433.
doi: 10.3390/ma15041433

38. Rouwkema J, Khademhosseini A. Vascularization and angiogenesis in tissue engineering: beyond creating static networks. *Trends Biotechnol*. 2016;34(9):733-745.
doi: 10.1016/j.tibtech.2016.03.002.

39. Carotenuto F, Politi S, Ul Haq A, De Matteis F, Tamburri E, Terranova ML, Teodori L, Pasquo A, Di Nardo P. From soft to hard biomimetic materials: tuning micro/nano-architecture of saffolds for tissue regeneration. *Micromachines*. 2022;13(5):1-25.
doi: 10.3390/mi13050780.

40. Zhang L, Yang G, Johnson BN, Jia X. Three-dimensional (3D) printed scaffold and material selection for bone repair. *Acta Biomater*. 2019;84(10):16-33.
doi: 10.1016/j.actbio.2018.11.039.

41. Li X, van Blitterswijk CA, Feng Q, Cui F, Watari F. The effect of calcium phosphate microstructure on bone-related cells in vitro. *Biomaterials*. 2008;29(23):3306-3316.
doi: 10.1016/j.biomaterials.2008.04.039.

42. Li X, Liu H, Niu X, Fan Y, Feng W, Cui FZ, F Watari F. Osteogenic differentiation of human adipose-derived stem cells induced by osteoinductive calcium phosphate ceramics. *J Biomed Mater Res B Appl Biomater*. 2011;97(1):10-19.
doi: 10.1002/jbm.b.31773.

43. Hernandez JL, Woodrow KA. Medical applications of porous biomaterials: features of porosity and tissue-specific implications for biocompatibility. *Adv Healthc Mater*. 2022;11(9):1-25.
doi: 10.1002/adhm.202102087.

44. Hayrapetyan A, Bongio M, Leeuwenburgh SCG, Jansen JA, van den Beucken JJJP. Effect of nano-HA/collagen composite hydrogels on osteogenic behavior of mesenchymal stromal cells. *Stem Cell Rev Rep*. 2016;12(3):352-364.
doi: 10.1007/s12015-016-9644-x.

45. Japudom J, Karaman S, Quartey BC, WMohamed WKE, Mahtani N, Garcia-Sabaté A, Teo J. Collagen fibril orientation instructs fibroblast differentiation via cell contractility. *Adv Sci*. 2023;10(22):1-14.
doi: 10.1002/advs.202301353.

46. Togo S, Sato T, Sugiura H, Wang X, Basma H, Nelson A, Liu X, Bargar TW, Sharp JG, Rennard SI. Differentiation of embryonic stem cells into fibroblast-like cells in three-dimensional type i collagen gel cultures. *Vitr Cell Dev Biol Anim*. 2011;47(2):114-124.
doi: 10.1007/s11626-010-9367-2.

47. Rivas M, Turon P, Alemán C, Puiggalí J, del Valle LJ. Incorporation of functionalized calcium phosphate nanoparticles in living cells. *J Clust Sci*. 33(1):2781-2795.
doi: 10.1007/s10876-021-02182-6.

48. Komatsu K. Mechanical strength and viscoelastic response of the periodontal ligament in relation to structure. *J Dent Biomech*. 2009;2010:502318. doi: 10.4061/2010/502318.

49. Takedachi M, Yamamoto S, Kawasaki K, Shimomura J, Murata M, Morimoto C, Hirai A, Kawakami K, Bhongsatiern P, Iwayama T, Sawada K, Yamada S, Murakami S. Reciprocal role of PLAP-1 in HIF-1α-mediated responses to hypoxia. *J Periodontal Res*. 2022:57(3):470-478. doi: 10.1111/jre.12976.

50. Knaup I, Symmank J, Bastian A, Neuss S, Pufe T, Jacobs C, Wolf M. Impact of FGF1 on human periodontal ligament fibroblast growth, osteogenic differentiation and inflammatory reaction in vitro. *J Orofac Orthop.* 2022;83(Suppl 1):42-55. doi: 10.1007/s00056-021-00363-6.

51. Gardeazabal L, Izeta A. Elastin and collagen fibres in cutaneous wound healing. *Exp Dermatol.* 2024;33(3):1-14. doi: 10.1111/exd.15052.

52. Schini M, Vilaca T, Gossiel F, Salam S, Eastell R. Bone turnover markers: basic biology to clinical applications. *Endocr Rev.* 2023;44(3):417-473. doi: 10.1210/endrev/bnac031.

53. Ogle ME, Segar CE, Sridhar S, Botchwey EA. Monocytes and macrophages in tissue repair: implications for immunoregenerative biomaterial design. *Exp Biol Med.* 2016;241(10):1084-1097. doi: 10.1177/1535370216650293.

54. Londono R, Dziki JL, Haljasmaa E, Turner NJ, Leifer, Badylak. The effect of cell debris within biologic scaffolds upon the macrophage response. *J Biomed Mater Res A*. 2017;105(8):2109-2118. doi: 10.1002/jbm.a.36055.

55. P Feng, R Zhao, W Tang, F Yang, H Tian, S Peng, H Pan, C Shuai. Structural and functional adaptive artificial bone: materials, fabrications, and properties. *Adv Funct Mater.* 2023;33(23):1-29. doi: 10.1002/adfm.202214726.

56. Levenberg S, Rouwkema J, Macdonald M, Garfein ES, Kohane DS, Darland DC, Marini R, Van Blitterswijk CA, Mulligan RC, D'Amore PA, Langer R. Engineering vascularized skeletal muscle tissue. *Nat Biotechnol.* 2005;23(7):879-884. doi: 10.1038/nbt1109.

57. Nagasaki K, Chavez MB, Nagasaki A, Taylor JM, Tan MH, Ma M, Ralston E, Thew ME, Kim DG, Somerman MJ, Foster L. The bone sialoprotein RGD domain modulates and maintains periodontal development. *J Dent Res.* 2022;101(10):1238-1247. doi: 10.1177/00220345221100794.

58. Chavez MB, Tan MH, Kolli TN, Zachariadou C, Farah F, Mohamed FF, Chu EY, Foster BL. Bone sialoprotein is critical for alveolar bone healing in mice. *J Dent Res.* 2023;102(2):187-196. doi: 10.1177/00220345221126716.

59. Candeliere GA, Liu F, Aubin JE. Individual osteoblasts in the developing calvaria express different gene repertoires. *Bone.* 2001;28(4):351-361. doi: 10.1016/S8756-3282(01)00410-0.

60. Chen J, Singh K, Mukherjee BB, Sodek J. Developmental expression of osteopontin (OPN) mRNA in rat tissues: evidence for a role for OPN in bone formation and resorption. *Matrix.* 1993;13(12):113-123. doi: 10.1016/s0934-8832(11)80070-3.

61. Xin Y, Xu P, Wang X, Chen Y, Zhang Z, Zhang Y. Human foreskin-derived dermal stem/progenitor cell-conditioned medium combined with hyaluronic acid promotes extracellular matrix regeneration in diabetic wounds. Stem Cell Res Ther. 2021;12(1):1-18. doi: 10.1186/s13287-020-02116-5.

62. Lee CH, Shah B, Moioli EK, Mao JJ. CTGF directs fibroblast differentiation from human mesenchymal stem/stromal cells and defines connective tissue healing in a rodent injury model. *J Clin Invest.* 2010;120(9):3340-3349. doi: 10.1172/JCI43230.

63. Becker W, Clokie C, Sennerby L, Urist MR, Becker BE, Histologic findings after implantation and evaluation of different grafting materials and titanium micro screws into extraction sockets: case reports. *J Periodontol.* 1998;69(4):414-421. doi: 10.1902/jop.1998.69.4.414.

64. Canellas JVDS, Ritto FG, C Figueredo CMDS, Fischer RG, de Oliveira GP, Thole AA, Medeiros PJD. Histomorphometric evaluation of different grafting materials used for alveolar ridge preservation: a systematic review and network meta-analysis. *Int J Oral Maxillofac Surg.* 2020;49(6);797-810. doi: 10.1016/j.ijom.2019.10.007.